AN ABSTRACT OF THE DISSERTATION OF

Jeff B. Schulte for the degree of Doctor of Philosophy in Physics presented on April 16, 2015.

Title: Hard Spheres Within Classical Density Functional Theory and Min Proteins in *Escherichia Coli*

Abstract approved: _____

David J. Roundy

This thesis reports on computational research in two different areas. I first discuss the Min-protein system found within *Escherichia coli*. Following this I discuss an extended investigation into improving free energy functionals that are used within Classical Density Functional Theory in order to model water.

Chapter 2 examines the dynamics of the Min-protein system within E. Coli, which aid in regulating the process of cell division by identifying the center of the cell. While this system usually exhibits robust bipolar oscillations in a variety of cell shapes, recent experiments have shown that when the cells are mechanically deformed into wide, flattened out, irregular shapes, the spatial regularity of these oscillations breaks down. We employ widely used stochastic and deterministic models of the Min system to simulate cells with flattened shapes. The

deterministic model predicts regular bipolar oscillations, in contradiction with the experimentally observed behavior, while the single molecule nature of the stochastic model, which is based on the same reaction-diffusion equations, leads to the disruption of the regular patterns of protein concentration. We further report on simulations of symmetric but flattened cell shapes, and find that it is the flattening and accompanying lateral expansion rather than the asymmetry of the cell shapes that causes the irregular oscillation behavior.

Chapter 3 begins our discussion of Classical Density Functional Theory research by introducing many of the key concepts used in the following chapters.

Chapter 4 investigates the value of the distribution function of an inhomogeneous hard-sphere fluid at contact. This quantity plays a critical role in statistical associating fluid theory, which is the basis of a number of recently developed classical density functionals, including ones developed within my research group. We define two averaged values for the distribution function at contact and derive formulas for each of them from the White Bear version of the fundamental measure theory functional, using an assumption of thermodynamic consistency. We test these formulas, as well as two existing formulas, against Monte Carlo simulations and find excellent agreement between the Monte Carlo data and one of our averaged distribution functions.

Chapter 5 details our modifications of our recently published statistical associating fluid theory-based classical density functional theory for water, incorporating this improved distribution function at contact. We examine the effect of this alteration by studying two hard-sphere solutes and a Lennard-Jones approximation

of a krypton-atom solute, and find improvement.

Finally, Chapter 6 introduces an approximation for the pair distribution function of the inhomogeneous hard sphere fluid. Our approximation makes use of the new distribution function at contact referred to above. This approach achieves greater computational efficiency than previous approaches by enabling the use of exclusively fixed-kernel convolutions, which allows for an implementation using fast Fourier transforms. We compare results for our pair distribution approximation with two previously published works and Monte Carlo simulation, showing favorable results.

Hard Spheres Within Classical Density Functional Theory and Min Proteins in *Escherichia Coli*

by

Jeff B. Schulte

A DISSERTATION

submitted to

Oregon State University

in partial fulfillment of
the requirements for the
degree of

Doctor of Philosophy

Presented April 16, 2015
Commencement June 2015

Doctor of Philosophy dissertation of Jeff B. Schulte presented on April 16, 2015.

APPROVED:

Major Professor, representing Physics

Chair of the Department of Physics

Dean of the Graduate School

I understand that my dissertation will become part of the permanent collection of Oregon State University libraries. My signature below authorizes release of my dissertation to any reader upon request.

Jeff B. Schulte, Author

ACKNOWLEDGEMENTS

I would like to express my deep appreciation and gratitude to my advisor, David Roundy, for his constant generosity, brilliance, and enthusiasm. This work wouldn't have been possible without him. I would also like to thank my committee members Ethan Minot, Yun-Shik Lee, and Henri Jansen, for their friendly guidance and their patience with me as I wound my way through the program. On my list as well are my colleagues Eric Krebs, Rene Zeto, Paho Lurie-Gregg, Patrick Kreitzberg, and Dan Roth for their contributions, conversations, and jokes. And finally my family, as always, for their never-failing support.

TABLE OF CONTENTS

TABLE OF CONTENTS (Continued)

LIST OF FIGURES

LIST OF FIGURES (Continued)

LIST OF FIGURES (Continued)

LIST OF FIGURES (Continued)

LIST OF FIGURES (Continued)

LIST OF TABLES

1 Introduction

My doctoral work at Oregon State University naturally divides along two avenues of research. I have contributed to three peer reviewed publications that fall within the realm of classical Density Functional Theory, which is the primary research area of my advisor, Dr. David Roundy. Along side of this I have also completed a research project in the realm of systems biology, in which I simulate the dynamics of the Min system of proteins within *Escherichia coli*.

Contrary to how this may appear, these two lines of research actually have quite a deal in common with each other. The basic concepts are really not too different, and many of the skills used in completing one also applied to the other. Both lines of research simulate complex systems using a three dimensional grid. In the case of DFT, we calculate thermodynamic densities as a function of space, while in the case of the Min project, we calculate protein densities, also as a function of space. The mathematics in both address interactions between the local densities and their neighbor densities, and both simulate microscopic interactions that result in macroscopic effects. The process of conducting both types of research requires working out basic conceptual models, than coding up interactions, then managing large data sets as the systems are simulated, and then plotting the data in various ways to reveal the behavior of the systems. Also, in both projects we do the bulk of our simulating in C++, the bulk of our plotting in python, and data management

using the same Linux tools.

In essence, the two lines of research were not very much different than each other at all, and moving from one to the other felt very natural. I therefore include them both in this dissertation.

2 Min Protein System in *Escherichia Coli*

This chapter discusses my biological simulation research. Section 2.1 introduces the subject and briefly provides a historical context for the work. Section 2.2 discusses the simulation model I use and outlines the program I've written. Sections 2.3 and 2.4 discuss the resulting data and our conclusions.

2.1 Introduction

It is vital that during the process of bacterial cell division a cell avoid minicelling, or splitting into daughter cells with lopsided volumes. Instrumental to this process in *Escherichia coli* is a long FtsZ polymer chain that develops on the cell wall in the center region of the cell, helping dictate the plane of division [10, 11]. Previous experimental studies have shown that the MinC protein, known to inhibit the FtsZ polymer [12], exhibits regular pole to pole oscillatory behavior between both ends of the wild-type pill-shaped cell. It thus has a higher time averaged concentration in the cell poles than in the center region, which aides in preventing the FtsZ from developing in the wrong region. The MinC is recruited to these poles by MinD, which itself interacts with another protein, MinE, in a system which exhibits pole-to-pole oscillatory behavior [1, 13–17].

Previous experimental studies have shown that the MinD protein system is

capable of exhibiting oscillations in round shapes [18, 19] as well as in connected three pronged tube shapes [20], in which the oscillations seem to seek out the extreme poles in the cell. Mannik *et al.* have recently shown that there are limitations to this robust capability to oscillate [2,17,21]. They have experimentally forced *E. coli* cells into microfabricated channels of thickness less than that of the natural diameter of the cells, in which they area able to grow and divide. Upon entering the channels, the cells undergo a mechanical deformation in which they both widen and lengthen within the plane of the channel. This deformation results in very wide (they can reach widths of over 5μm) flattened cells that when viewed from the top down have irregular and asymmetric shapes. While these cells are still able to divide into surprisingly equal volumes, the MinD oscillations in these cells are spatially irregular. Seen with fluorescent microscopy, the MinD maximize in multiple locations within the cell, in a seemingly random sequence. These experiments allow for an opportunity to test theoretical models of the MinD system against more extreme experimental cases than have been seen thus far. An additional interesting question is whether the irregularity observed by Mannik *et al.* indicates that the MinD system can become chaotic (as in e.g. Ref. 22), or if this irregularity is the result of a stochastic but nonchaotic process.

A number of models of the MinD protein system have been developed that accurately describe its basic oscillatory nature. Early models involved free proteins that affect each others' rates of diffusion and membrane attachment, but do not combine into compound states [23]. In 2003 Huang improved upon this approach with a simple and very successful simulation model based on MinD-MinE

combination, ATPase hydrolysis, and MinD membrane attachment that exhibits accurate MinD oscillations in cylindrical cells [1]. In this model cytoplasmic MinD is recruited to the membrane by MinD that is already clustered there (following observed non-linear attachment of MinD on the cell membrane [24, 25]), and is stationary once attached.

Several models [19, 26, 27] modify Huang's original model to more accurately reflect experimental findings, which were published after his 2003 paper [28, 29]. These models introduce diffusion along the membrane that is two to three orders of magnitude slower than that within the cytoplasm, and increase the rate of cytoplasmic diffusion by a factor of about five, reflecting an experimental measurement of these parameters [28]. They also increase or assume instantaneous [26] the nucleotide exchange rate. In addition, they revise the process of MinD recruitment to the membrane, removing recruitment of MinD to the membrane by MinD-MinE complexes, behavior that has not been observed experimentally. The model of Bonny *et al.* further more allows MinE to remain independently attached to the membrane after disassociating with MinD [26].

There are only on the order of a thousand MinD proteins in a given cell, which is fewer than the number of grid points used in our simulations, suggesting that the deterministic continuum description–which requires fractional numbers of proteins at each grid point—may break down, and that stochastic behavior may play a significant role. To treat this, there have been a number of variations of the Huang 2003 model that stochastically simulate the similar reaction-diffusion equations [16, 19]. These studies largely confirm the results of Huang's deterministic model when

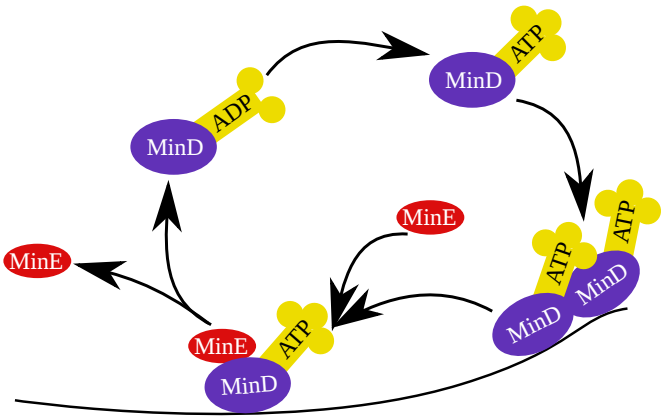

Figure 2.1: Reactions included in the model of Huang *et al.* [1].

applied to the wild-type, pill-shaped phenotype. However, the stochastic models are slightly more successful in predicting experimentally observed oscillations in round cell phenotypes [19, 30], and they enable prediction of fluctuations in the predicted behavior [31]. Both deterministic and stochastic models are widely used throughout systems biology [32–36], and have unique advantages and limitations. The deterministic approach has an advantage in providing a simple prediction of average behavior, while the stochastic approach enables prediction of fluctuations from that mean, and reduces sensitivity to initial conditions.

In this paper we use Huang's original 2003 model [1], which has been widely used [16, 30, 37] in both deterministic and stochastic variants, to study flattened cells of 0.4μm thickness that are similar to those observed by Mannik *et al.* [17].

2.2 Materials and Methods

Model and Cell Shapes

We implement the reaction-diffusion model of Huang *et al.* [1]. Figure 2.1 shows the reaction process. The cytoplasmic MinD:ADP complex undergoes nucleotide exchange and is changed into the MinD:ATP complex. This will naturally diffuse and attach to the cell membrane. A cytoplasmic MinE will attach to the wall bound MinD:ATP complex and after a time will activate ATP hydrolysis. This breaks up the complex, releasing MinE, phosphate, and MinD:ADP back into the cytoplasm. The MinD:ADP will undergo nucleotide exchange and begin again the cyclic process. The model is defined by a set of five reaction-diffusion equations:

$$\frac{\partial \rho_{D:ADP}}{\partial t} = \mathcal{D}_D \nabla^2 \rho_{D:ADP} - k_D^{ADP \to ATP} \rho_{D:ADP} + \delta(d_w) k_{de} \sigma_{DE}, \tag{2.1}$$

$$\frac{\partial \rho_{D:ATP}}{\partial t} = \mathcal{D}_D \nabla^2 \rho_{D:ATP} + k_D^{ADP \to ATP} \rho_{D:ADP} - \delta(d_w)[k_D + k_{dD}(\sigma_D + \sigma_{DE})] \rho_{D:ATP} \tag{2.2}$$

$$\frac{\partial \rho_E}{\partial t} = \mathcal{D}_E \nabla^2 \rho_E + \delta(d_w) k_{de} \sigma_{DE} - \delta(d_w) k_E \sigma_D \rho_E \tag{2.3}$$

$$\frac{\partial \sigma_D}{\partial t} = -k_E \sigma_D \rho_E + [k_D + k_{dD}(\sigma_D + \sigma_{DE})]\rho_{D:ATP} \tag{2.4}$$

$$\frac{\partial \sigma_{DE}}{\partial t} = -k_{de} \sigma_{DE} + k_E \sigma_D \rho_E \tag{2.5}$$

where ρ is cytoplasmic protein density (proteins/μm^3), σ is membrane bound density (proteins/μm^2), $\mathcal{D}_D$ and $\mathcal{D}_E$ are the diffusion constants for MinD and MinE, respectively, $k_D^{\mathrm{ADP} \to \mathrm{ATP}}$ is the rate of conversion from MinD:ADP to the MinD:ATP complex, k_D is the rate of MinD:ATP attachment to the membrane when no protein is already attached there, k_{dD} is the increase of this rate when MinD:ATP is present on the membrane, k_{de} is the rate of hydrolysis of the MinD:MinE:ATP complex, k_E is the rate of cytoplasmic MinE binding to membrane bound MinD:ATP complex, and d_w is the distance from the point in space to the closest wall. The Dirac delta function $\delta(d_w)$, which we need to describe the location of the membrane, has units of μm^{-1} and is zero everywhere except at the wall. Equations 2.4 and 2.5 are only relevant at the membrane because the membrane-bound density values have no meaning in the cytoplasm.

Our diffusion and reaction rates are shown below. We are interested primarily in the effect of cellular size and shape on the protein oscillations, so we use Huang's parameter values [1].

$$\mathcal{D}_D = \mathcal{D}_E = 2.5\mu\text{m}^2/\text{sec}$$

$$k_D^{\text{ADP} \to \text{ATP}} = 1/\text{sec},\ k_D = 0.025\mu\text{m}/\text{sec}$$

$$k_{dD} = 0.0015\mu\text{m}^3/\text{sec},\ k_{de} = 0.7/\text{sec}$$

$$k_E = 0.093\mu\text{m}^3/\text{sec}.$$

Huang's simulations use total MinD and MinE concentrations of $1,000/\mu$m and $350/\mu$m, respectively, in a cylindrical cell of radius 0.5μm, and in our (non-cylindrical) cells we use the same number of proteins per unit volume. These concentration values are $1273\mu\text{m}^{-3}$ and $446\mu\text{m}^{-3}$, respectively. We have written our own simulation platform and membrane creation tools from scratch, instead of using existing available software used in previous studies [16, 19, 26, 27]. Our simulations take place within a three-dimensional Cartesian grid that has a grid spacing of $.05\mu$m, and our cell shapes are specified as the zero of an analytic function which can generate the geometry presented in this paper. This code is publicly available on github [38], including scripts that generate the simulation data used in this paper.

We have performed both a numerical, deterministic model simulation that is spatially and temporally discrete, and a stochastic simulation that is spatially discrete but continuous in time. Our stochastic model follows the work of Kraus [39] which in turn follows a method introduced by Gillespie [40].

We mean to investigate the geometric limits of the Min system oscillations as

observed by Mannik *et al.* [2], so we have modeled the Min system in several cell shapes and sizes. Here we present a selection of these, beginning with naturally occurring pill-shaped cells, followed by a number of flattened out shapes which reflect the experiments of Mannik *et al.*, in which bacteria are confined within thin slits. These slits are fabricated with a width of .25μm, but they are coated with a PDMS lining that the cells are able to deform, raising uncertainty in the actual cell thickness. Tests with pure silicon, non-deformable slits show that the smallest thickness for which cells are able to penetrate is .4μm [2, 17]. We therefore assume that the PDMS slits have been deformed to this thickness and simulate flattened cells with a thickness of .4μm. Viewed from the top down the cells have the shapes described below and viewed from the side they have at their edges a semicircular cross-section (one may imagine the shape of a pancake). In this paper we focus on four specific flattened cell shapes. Two of these shapes replicate those published by Mannik *et al.*, and the other two are 'stadium' shapes that respectively have the same aspect ratio, thickness, and volume as the two cell shapes experimentally observed by Mannik *et al.* [2]. Viewed from the top down, these stadium shapes appear as rectangles with semi-circular end caps on the long axis ends.

Huang *et al.* [1] have performed a linear stability analysis on a cylindrical model which shows an upper limit on a steady state solution of a 2μm half wavelength. Cells with dimensions longer than this spontaneously develop spatial oscillations, while cells that are shorter relax into a homogeneous steady state. We have performed a similar linear stability analysis on an infinite slab with a thickness equal to that of our flattened cells (0.40μm). We first solve the model's five differential

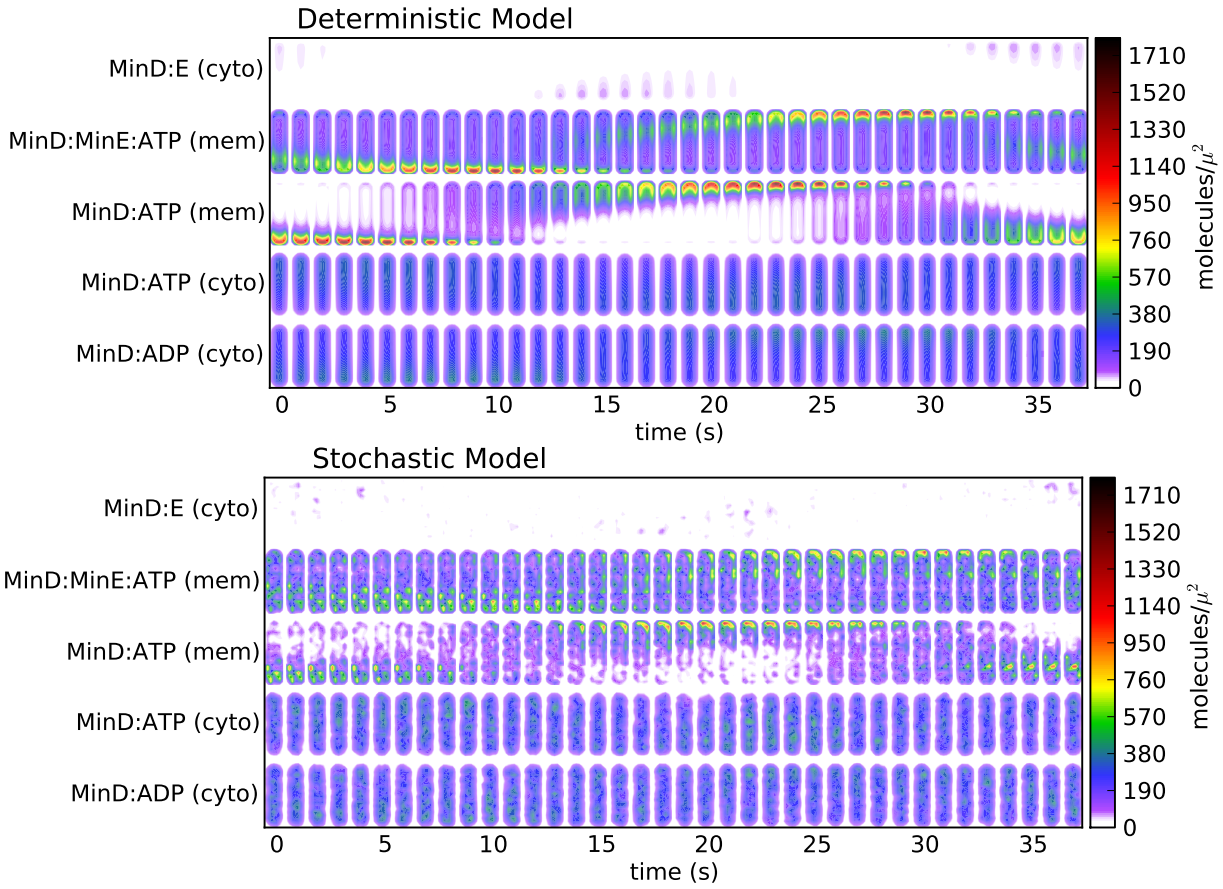

Figure 2.2: Images of the concentration of each protein species in a natural pill-shaped bacterium at one-second time intervals. The upper plots shows results from the deterministic model and the lower shows results from the stochastic model. The order of frames is such that individual MinD proteins begin at the bottom of the plot (in the MinD:ATP state in the cytoplasm), and progress upward until they reach the MinE:MinD:ATP membrane-bound complex. At that point, they will spontaneously dissociate into cytoplasmic MinE (the top row) and the starting state of cytoplasmic MinD:ADP.

.

equations for the steady state solution, under the constraint that the total number MinD and MinE molecules matches our simulation. We write down as a matrix the linear response of the time derivatives of the density to small, spatially harmonic density perturbations around the steady-state density. The system is stable at this wavelength provided all eigenvalues of the matrix are negative, indicating that all perturbations with this wavelength will decay. We find the stability limit by searching for the largest wavelength at which the system is stable. Through this method we arrive at an upper half wavelength stability limit of 1.56μm for our 0.40μm flattened cells. As expected, when decreasing the lengths and widths of our simulated flattened cells so that the longest distance across the cell is less than this length, the cells stop exhibiting any oscillatory behavior. The deterministic model relaxes into a motionless state and the stochastic model exhibits random fluctuations without spatial oscillations.

2.3 Results and Discussion

Naturally Occurring Pill Shaped Cells

We begin with the naturally occurring pill cell shape. We piece this shape together as a cylinder with hemispherical end caps. This shape follows the early simulations of Huang *et al.* but differs in that we have added the end caps for a more natural shape, expecting similar results.

Figure 2.2 shows a series of color plots of the density of proteins at each stage

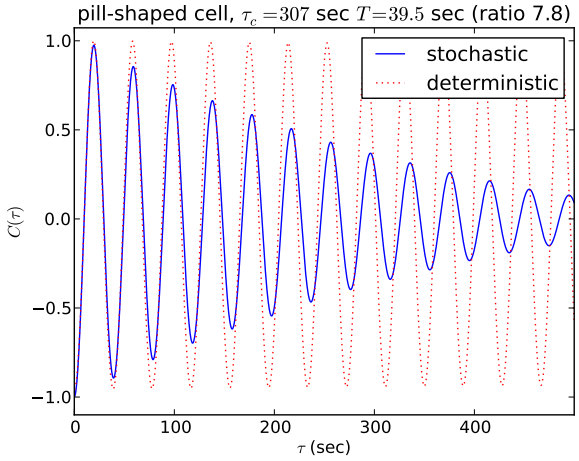

Figure 2.3: Temporal correlation function of the total MinD found in two opposite polar regions of the pill-shaped cell, shown against the correlation time. Data for both the the deterministic and stochastic models are shown. The stochastic model shows an oscillation period of 39.5 seconds and coherence time of 307 seconds. The correlation functions are scaled to have the same initial value.

of the reaction cycle. Deterministic simulation data is shown above and stochastic simulation data is shown below. The cells shown are 4μm in length, measured from end to end. We have 'smeared out' the stochastic concentrations in a manner meant to reproduce the images shown by diffraction limited fluorescence microscopy. We do so using the two dimensional Gaussian approximation developed by Zhang *et al.* [41]. In this approximation we use a numerical aperture value of 1.3, which is the same as used by Mannik experimentally, and a wavelength of $650nm$. Each frame is 2.5 seconds ahead of the last, and each image shows the concentration of a given state of protein (of the five described in the reaction model) summed over the coordinate normal to the page.

Figure 2.2 begins about 300 seconds into the simulation and shows one period of oscillation. At $t = 0$ there is a high concentration of MinD:ATP that has accumulated on the membrane at the bottom of the cell. An important aspect of Huang's model is that the MinD is attracted to and sticks to the membrane non-linearly: as it accumulates there it begins to 'recruit' other MinD that is diffusing in the cytoplasm nearby, causing peaks in concentration to build up on the walls. Meanwhile, the MinE creeps downward as it reacts with the membrane-bound MinD, forming the MinD:MinE:ATP complex, then breaks it apart and diffuses downward a bit more before it again reacts with membrane-bound MinD. This process can be seen in the form of the well-known "MinE rings" (actually, MinE bound to MinD on the membrane). These rings are visible in the deterministic model plots as a green band on the walls from 0 seconds to 4 seconds (and later from 15 to 23 seconds). The appearance of these rings in the deterministic model

alongside their less obvious appearance in the stochastic model highlights an advantage of the deterministic model: the idealization of deterministic data allows one to see patterns in the averaged behavior that might otherwise be missed. In the stochastic model the MinE still exhibits higher concentrations in the same regions throughout the process, but what would ideally be a "ring" pattern is instead an asymmetric collection of maxima, which would become a ring after phase-locked averaging.

During the formation of these rings, cytoplasmic MinE is diffusing in the upper portion of the cell and will naturally progress downward, where there is membrane-bound MinD to react with, leading to a depletion of MinE in the upper portion of the cell. As the MinE ring converges upon the lower end of the cell, MinD that has been released is able to diffuse upward, past the ring, while still in its MinD:ADP state and unable to bind to the membrane. After it undergoes nucleotide exchange, resulting in MinD:ATP, it is ready to accumulate on the walls in at the top of the cell, where the MinE has been depleted. This can be seen in seconds 10 through 20 in both models, followed by the subsequent MinE ring formation and movement upward (beginning the same process in the opposite direction) that can be seen in seconds 15 through 23.

Both Fig. 2.2 and its associated movies, show that the stochastic model exhibits a "starry night" effect characterized by spatially fixed points of protein density build up, as recruitment leads to clusters of MinD forming on the wall and then subsequently dissipating. This results from the omission of diffusion along the membrane from Huang's model, which would allow these recruitment clusters

to spread out. Experiments have confirmed that diffusion along the membrane does occur, albeit with a rate two orders of magnitude lower than that in the cytoplasm [15]. The 'stars' in the effect typically last for around 10 seconds. The membrane-bound proteins will diffuse by a distance of around one micron during this time, which is enough to spread out across the polar section of the one micron diameter wild-type pill cells. As we see below, the flattened, irregular cells are large enough that this one micron blurring would not completely eliminate this 'starry night' effect.

We also analyze the temporal periodicity of the system, which we quantify with the temporal correlation function of the total MinD found in two opposite polar regions. This correlation function, which is displayed in Fig. 2.3, is given by

$$C(\tau) \propto \int (N_{top}(t) - \bar{N}_{top})(N_{bottom}(t+\tau) - \bar{N}_{bottom})dt \tag{2.6}$$

where $N_{top}(t)$ and $N_{bottom}(t)$ are the total MinD proteins in the top and bottom thirds of a cell. These plots help us in studying the periods and the regularity and stability of oscillations. These curves are well fit with a simple decoherence model, given by the equation

$$C(\tau) = -\cos\left(\frac{2\pi\tau}{T}\right) e^{-\frac{\tau}{\tau_c}} \tag{2.7}$$

where T is the period and τ_c is the coherence time. In the case of the stochastic model the pill exhibits coherence times of about 8 periods, indicating that the system exhibits periodic oscillation, with some stochastic irregularity in the period. In contrast, in the deterministic model the pill-shaped cell exhibits complete

coherence, indicating that its behavior is perfectly periodic.

Comparison of Experimental and Stadium Shapes

As explained above, we focus on simulation of four illustrative flattened cell shapes: two shapes created to replicate those shapes observed experimentally by Mannik *et al.* [2] (shape A and shape B), and for comparison two 'stadium' shapes that have the identical aspect ratio, thickness and volume (stadium A and stadium B), shown in Figure 2.4. All of the flattened cells have lost the rotational symmetry of the original pill shapes, but while shape A and shape B have only one mirror plane symmetry (that is normal to the flattened plane), stadium A and stadium B have three. This allows us to distinguish between the effect of flattening the cell and the cell shape's irregularity and asymmetry.

From each of these flattened simulations, we have chosen a typical 350 second segment to compare with the published results of Mannik *et al.* [2], exemplified in arrow plots in which the arrow heads show the location of sequential MinD maxima within the cell (in Fig. 2.4). In addition to arrows between successive maxima in space and time, we plot as a colored background the density of MinD proteins averaged over the same time period. We note that we have manually verified that our (computer-generated) arrow plots also reflect a human interpretation of a movie of the same data. Finally, for comparison we present the same plot for a wild-type cell, with a time period of 250 seconds to account for its short period of oscillation.

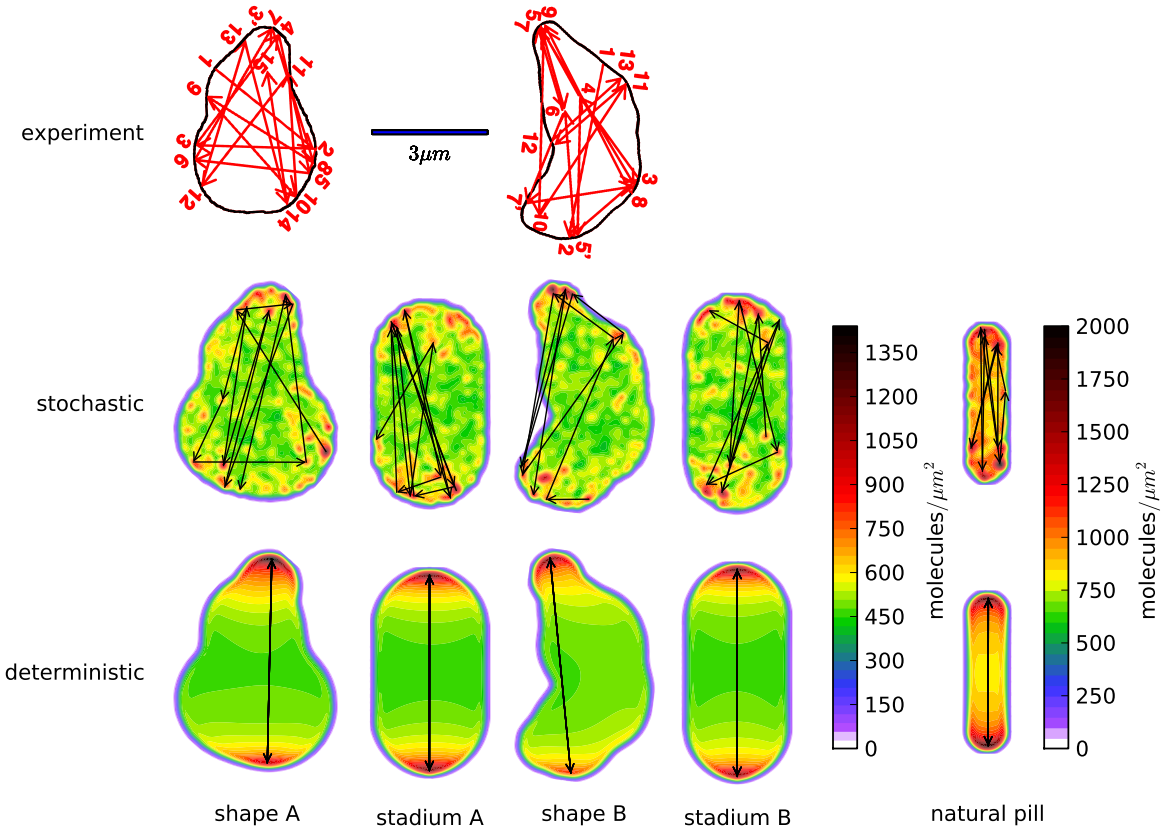

Figure 2.4: We display here arrows depicting successive maxima in space and and time overlayed on a color plot of the total MinD density averaged over the same time period. The simulation time covered for the flattened cells is 350 seconds, which is the same period of time depicted in the experimental data plots of Mannik *et al.* [2]. For the wild-type pill shape, we only cover 250 seconds, in order to provide a useful comparison due to its shorter oscillation period. The top row shows plots published by Mannik *et al.* of the MinD maxima behavior and the bottom two rows show our simulations using the stochastic and deterministic models, respectively. We simulated approximations to the two shapes observed by Mannik, which we call *shape A* and *shape B*. In addition, we studied two flattened stadium shapes which we call *stadium A* and *stadium B* corresponding in aspect ratio and thickness to the two experimental shapes. The spatial length scale of all the figures shown was identical. Each of the flattened cell shapes uses the same color scale for the number of proteins per unit area. Finally, we display the natural pill shape, which was also featured in Figs. 2.2 and 2.3, with a different color scale to reflect the thicker cell containing more proteins per cross-sectional area.

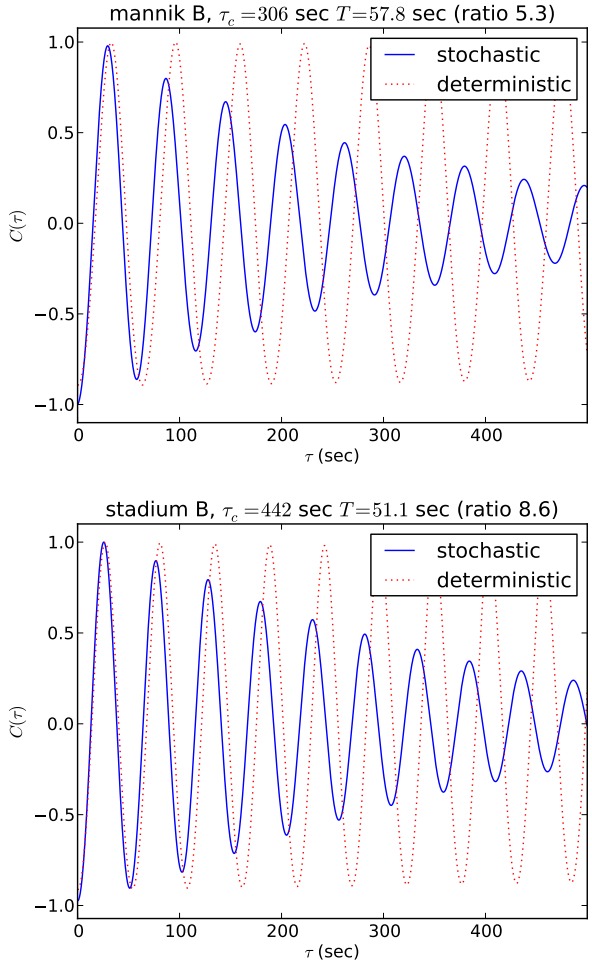

Figure 2.5: Temporal correlation function of the total MinD found in two opposite polar regions of the shape B (above) and the stadium B (below) cell shapes, shown against the correlation time. Data for both the the deterministic and stochastic models are shown, and the correlation functions are scaled to have the same initial value. For shape B, the stochastic model shows an oscillation period of 58 seconds and coherence time of 306 seconds, so that it takes roughly 5.3 periods for the behavior to decohere. For the stadium B, the same model shows an oscillation period of 51 seconds and coherence time of 442 seconds, so that it takes roughly 8.6 periods for the behavior to decohere.

In every case, including the wild-type pill shape, we see irregularity in the location of the maxima when using the stochastic model. The deterministic model shows uniformly bipolar oscillation. We conclude that the model is *not* chaotic (which would show irregularity in the deterministic computation), but rather that the irregularity results purely from stochastic processes. From these results and how they compare with experiment, we conclude that the deterministic model is inadequate to explain experimental observations of the locations of density maxima of the MinD protein.

The predictions of the stochastic model are roughly similar to the experimental results in terms of irregularity of the locations of maxima, although there are locations on the edges of the cells where experiment shows maxima occurring that we never see in our simulations, suggesting that the model does not precisely reflect the experiment. We also note that the stadium shapes in Fig. 2.4 appear to have maxima location irregularity that is qualitatively similar to our irregular shapes and to experiment.

However Fig. 2.4 leaves unclear the importance of the flattening and accompanying lateral expansion of the cell versus cell shape irregularity and asymmetry in the temporal regularity of the oscillations. Although in the movies the stadiums appear to display, on average over long time scales, a somewhat more regular oscillation than appears in the irregular shapes A and B, the limited time range of the arrow plots (350 seconds) is inadequate to make this comparison. We therefore return to the correlation function between the number of proteins in a segment at the top of the cell and the number of proteins in a segment at the bottom of the

cell. Fig. 2.5 shows this plot for shape B and stadium B. Here we plot correlations of correlation times up to 500 seconds, a biologically relevant timescale. E. Coli cell doubling times vary widely depending on environmental conditions, but will often be between 20 minutes to 100 minutes [42], while fluorescent microscopy experiments have shown that the FtsZ ring builds itself with a half life of roughly 30 seconds [43].

We see that both in the shape B and stadium B, the deterministic model is perfectly periodic. Both the deterministic and stochastic model correlations have the same number of proteins in their cells, and have been normalized with the same normalization factor, so that they can be directly compared against each other. The stochastic simulation of shape B has a coherence time of 5.3 periods, while the corresponding simulation of stadium B has a coherence time of 8.6 periods. The correlation function for stadium A is similar to that of stadium B, with similar coherence time (13 periods, not shown), while shape A also exhibits a similar coherence time (5.5 periods). This confirms that the stadium shapes do indeed oscillate somewhat more regularly than the irregular shapes, but both are comparable to the wild-type pill shape. From the stochastic correlation data, we conclude that irregularity of shape has only a moderate affect on the temporal regularity of the oscillatory behavior, with even the very distorted shape B exhibiting only a factor of two greater decoherence.

2.4 Conclusion

We find agreement between our stochastic simulations and experiments showing disrupted bipolar MinD oscillation in asymmetric flattened E. coli cells [2]. As observed experimentally, our simulations predict that MinD maxima will form in a spatially irregular sequence of locations. This result builds upon existing results showing that this model and its variants are effective in a variety of wild-type and mutated cell shapes [19,20,31], and reinforces that stochastic variations of Huang's 2003 model [16, 19] has considerable predictive power beyond the standard wild-type cell.

In contrast to the stochastic model, the original deterministic version of the model [1] predicts behavior that contradicts experimental observations. Specifically, the deterministic model predicts robust and periodic bipolar oscillation in irregularly shaped cells. Thus we conclude that this method is inconsistent with experiment, and cannot be relied upon for predictions of the behavior of the MinD system. This is the most clear example of the inadequacy of the deterministic simulation method in reproducing experimental behavior of the MinD system to date. Until now the results of deterministic and stochastic simulation have largely coincided, with the stochastic method showing minor differences in behavior when compared to deterministic models [16,19,30,31]. The regular oscillations in the deterministic case also allow us to conclude that the model is non-chaotic. Because of their similar construction, we anticipate that recent variants of the model [19,26,27] would also prove to be non-chaotic.

We find that flattened but regular and symmetric cells exhibit MinD oscillations that are qualitatively similar to the oscillations observed experimentally (and in our simulation) in irregular and asymmetric cells. This demonstrates that asymmetry is not required in order to induce spatially irregular MinD oscillations. In addition, the temporal regularity of oscillations is only moderately affected by irregularity in the shape of flattened cells. Thus we conclude that it is the flattening of the cells, and the accompanying expansion in the transverse direction, rather than their irregular shape that primarily causes the disruption of regular bipolar oscillation which is observed by Mannik *et al.* [2].

3 Introduction to Classical DFT Research

We now move away from systems biology and into my research in Classical Density Functional Theory. This chapter provides a general introduction to the concepts that are used in the three projects to which I contributed. I tried to write it as a primer for the following chapters, which discuss each of the three projects individually. It is intended to be accessible to physicists with no familiarity with the theory of liquids, and should provide the back round needed for the following chapters.

3.1 Classical Density Functional Theory

A classical statistical ensemble is a collection of microstates that share certain macroscopic properties, but have an otherwise appropriately random distribution of positions and momenta. In the canonical ensemble, the number of particles N, the total volume of the system V, and the temperature T are constant. In this ensemble the free energy, defined as $F = U - TS$, where U is the internal energy and S is the entropy of the system, is minimized in thermodynamic equilibrium. In the grand canonical ensemble, the number of particles is allowed to vary while V, T and the chemical potential μ are constant. In this ensemble it is the grand potential, defined as $\Omega = F - \mu N$, that is at a minimum in thermodynamic equilibrium.

In the case of inhomogeneous fluids, a treatment of the inhomogeneous external

potential $\phi(\mathbf{r})$ affects the positions of the particles in the system and stands in the place of the volume V in the thermodynamic equations. In such a system, a change in the internal energy is

$$\delta U = T\delta S + \int \delta n(\mathbf{r})\phi(\mathbf{r})d\mathbf{r} + \mu\delta N \tag{3.1}$$

where $n(\mathbf{r})$, which I will refer to as the 'density profile', is discussed in the next subsection.

3.1.1 Discussion of the density profile $n(\mathbf{r})$

Because our work deals very heavily with the concepts associated with particle density, it's worthwhile to discuss these concepts specifically.

One can define $n(\mathbf{r})d\mathbf{r}$ as the average number of particles at $\mathbf{r}$ within a volume $d\mathbf{r}$. I'll define it throughout this document in this fashion (as one does when working in Classical DFT), but the reader should be aware that during the DFT process, this definition is not always strictly accurate. As I'll discuss below, one of the steps of Classical DFT is to minimize the grand potential function, and during this process, $n(\mathbf{r})$ is actually often a 'trial density profile' or 'possible density profile' as opposed to the physical equilibrium density profile. However, after the function has been minimized and a thermodynamic solution has been reached, $n(\mathbf{r})d\mathbf{r}$ is indeed the average number of particles found in the volume $d\mathbf{r}$ in thermal equilibrium. For our purposes, we can always define in this way.

The density profile $n(\mathbf{r})$ is actually the one particle limit of a more general multi-particle density. In the grand canonical ensemble, this multi-particle density can be calculated as

$$n^{(n)}(\{\mathbf{r}^n\}) = \frac{1}{\Xi}\sum_{N=n}^{\infty}\frac{\exp(N\beta\mu)}{\Lambda^3(N-n)!}\int\exp(-\beta V_N)d\mathbf{r}^{(N-n)}. \tag{3.2}$$

$n^{(n)}(\{\mathbf{r}^n\})$ has the general form of a statistical mechanical probability, with an integration over possible states of Boltzmann factors divided by the grand canonical partition function,

$$\Xi = \sum_{N=0}^{\infty}\frac{\exp(N\beta\mu)}{h^{3N}N!}\int\int\exp(-\beta\mathcal{H})d\mathbf{r}^N d\mathbf{p}^N. \tag{3.3}$$

V_N in Eq. 3.2 is the total interaction potential between all of the particles in the system, and the spatial integral is taken over all the potential positions of the particles *other* than the superscript n particles at positions $\mathbf{r}^n$. Chapters 4 and 6 refer to the two particle limit of this function, the 'pair density' profile, $n^{(2)}(\mathbf{r}_1, \mathbf{r}_2)$. The $\exp(N\beta\mu)$ term in Eq. 3.2 accounts for the chemical potential's regulation of the average number of particles in the system. When implementing density functional theory, one adjusts μ in order to constrain the system's average number of particles,

$$\int_{system} n(\mathbf{r})d\mathbf{r} = \langle N\rangle \tag{3.4}$$

to be a desired value.

3.1.2 Summary of derivation of Classical Density Functional Theory

Using Classical DFT involves creating free energy functionals of the density profile, finding the density profile that minimizes the grand potential energy, and then of course running test after test to see how things went. I could just write that this is what we do and then define the terms, but I'd like to give an idea of *why* we do these things, so I'll discuss in this subsection a derivation of the theory. While the theory was originally derived and published in 1965 by Mermin [44], I use here the notation of Hansen [45].

The probability density, which is closely related to the n-particles density, is $f_0(\mathbf{r}^N, \mathbf{p}^N; N)$. $f_0(\mathbf{r}^N, \mathbf{p}^N; N)d\mathbf{r}^N$ is the probability that there are N particles in the system and that those particles are found within the infinitesimal range of positions $\mathbf{r}^N$ and momenta $\mathbf{p}^N$. Its definition is

$$f_0(\mathbf{r}^N, \mathbf{p}^N; N) = \frac{\exp(-\beta(\mathcal{H} - N\mu))}{\Xi} \tag{3.5}$$

where Ξ is once again the grand canonical partition function.

Classical DFT assumes that the Hamiltonian can be split into linearly combined parts:

$$\mathcal{H}(\mathbf{r}^N, \mathbf{p}^N) = K_N(\mathbf{p}^N) + V_N(\mathbf{r}^N) + \sum_{i=1}^{N} \phi(\mathbf{r}_i) \tag{3.6}$$

The three terms on the right are the kinetic energy, potential interaction between particles, and external potential, respectively. The kinetic energy is a function of

only the momenta of the particles, and the two potentials are functions of only their positions.

Substituting this for the Hamiltonian term in Eq. 3.5 and taking the natural logarithm, we have:

$$\ln f_0 = \beta\Omega - \beta K_N - \beta V_N - \beta \sum_{i=1}^{N} \phi(\mathbf{r}_i) + N\beta\mu \tag{3.7}$$

where we have used the relation

$$\Omega = -k_B T \ln \Xi, \tag{3.8}$$

which is the basic connection between thermodynamics and statistical mechanics in the grand canonical ensemble.

Eq. 3.7 is true for each microstate. We can relate this equation to the density profile by averaging over all the micro states in an ensemble. Because the external potential $\sum_{i=1}^{N} \phi(\mathbf{r}_i)$ and μ are both constant and $n(\mathbf{r})$ is the average ensemble equilibrium density at $\mathbf{r}$, the two right most terms average to

$$\langle \Phi_N \rangle = \int n(\mathbf{r})\phi(\mathbf{r}) d\mathbf{r} \quad \text{and} \quad \langle N\mu \rangle = \mu \int n(\mathbf{r}) d\mathbf{r} \tag{3.9}$$

Using these relations, taking the average of Eq. 3.7, and switching terms around results in the equation

$$\langle K_N + V_N + k_B T \ln f_0 \rangle \; = \Omega - \int n(\mathbf{r})\phi(\mathbf{r}) d\mathbf{r} + \mu \int n(\mathbf{r}) d\mathbf{r} \tag{3.10}$$

The thermodynamic definition of the grand potential gives us $F = \Omega + \mu N$. From this we can see that the right hand side of Eq. 3.10 is analogous to the free energy of the inhomogeneous system minus the energy due to the external potential. We call this function the 'intrinsic free energy' $\mathcal{F}$ since it only includes the interaction energy between the particles within the system (but not the external potential):

$$\mathcal{F} = \Omega - \int n(\mathbf{r})\phi(\mathbf{r})d\mathbf{r} + \mu \int n(\mathbf{r})d\mathbf{r} \ = \langle K_N + V_N + k_B T \ln f_0 \rangle \tag{3.11}$$

It can be shown [44, 45] that for a given μ, T, and defined function V_N describing the potential interaction between particles, there is a one-to-one relation between the external potential function and the equilibrium density profile $n(\mathbf{r})$ at thermodynamic equilibrium. The grand canonical density function f_0 (Eq. 3.5) for a given function V_N, μ, and T is a function of only the external potential, so as a result it is completely determined by $n^{(1)}$. V_N is also wholly determined by $n^{(1)}$ and K_N is determined by temperature. Thus the right hand side of Eq. 3.11 is a function of only the external potential and therefore also of only $n^{(1)}$, which means that for a given μ, T, and defined function V_N, $\mathcal{F}$ is wholly determined by $n(\mathbf{r})$.

Thanks to all of this, we can write

$$\Omega_\phi[n(\mathbf{r})] = \mathcal{F}[n(\mathbf{r})] + \int n(\mathbf{r})\phi(\mathbf{r})d\mathbf{r} - \mu \int n(\mathbf{r})d\mathbf{r} \tag{3.12}$$

where $n(\mathbf{r})$ is a density profile that we will adjust systematically in order to minimize $\Omega_\phi[n(\mathbf{r})]$. The function $n(\mathbf{r})$ that minimizes $\Omega_\phi[n(\mathbf{r})]$ becomes the minimized grand potential of the system, and the density profile $n(\mathbf{r})$ of the system is the density profile in thermodynamic equilibrium. It is finding this density profile in thermodynamic equilibrium, and then the properties that can be derived from it, that is the ultimate goal of Classical Density Functional Theory.

We begin the process of Classical DFT by designing the functional form of an approximation for the intrinsic free energy $\mathcal{F}$. This is the major theoretical part of the process. We then decide upon an external potential $\phi(\mathbf{r})$ that defines the external restrictions of the system we wish to examine, set the temperature T and chemical potential μ, and systematically adjust the density profile until we have found the global minimum of this grand potential. I won't discuss the process of finding the density profile that minimizes the grand potential in this dissertation, except to say that it is performed with standard methods such as conjugate gradient minimization. My research has been centered around the first part of the process, namely constructing the functional form for $\mathcal{F}$.

3.2 Introduction to SAFT and explanation of first free energy term

Work on Classical Density Functional Theory for inhomogeneous fluids involves creating the intrinsic free energy functional of the density profile, $\mathcal{F}[n(\mathbf{r})]$. This is typically written as a sum of terms that individually address different conceptual aspects of the system. Terms that treat different types of interaction between particles are added to the free energy of a reference system.

The free energy functional that we use in much of our work is one of a widely used family of models in the development of classical density functionals called Statistical Associating Fluid Theory (SAFT) [46]. SAFT is a theory for liquids based on a model of hard spheres with weak dispersion interactions and hydrogen-bonding association sites, which has been used to accurately model the equations of state of both pure fluids and mixtures over a wide range of temperatures and pressures [47, 48]. We will discuss the concept of hard spheres in detail in the following sections.

A SAFT functional is broken into the following terms:

$$\mathcal{F}_{SAFT} = F_{ideal} + F_{hardsphere} + F_{association} + F_{chain} + F_{dispersion} \tag{3.13}$$

We will discuss the meaning of these terms below in much more detail, but write them down now to illustrate the general structure of the total functional.

Although we work specifically with the SAFT functionals, our contributions described in the chapters 4, 5, and 6 are applicable to many different types of fluid functionals. Chapter 4 details a functional that we've created, the distribution

function at contact $g_\sigma(\mathbf{r})$, which accurately describes correlations between particles within a system, while chapter 5 discusses its use within a specific SAFT functional and its effect upon that functional's results. Chapter 6 introduces another function, the pair distribution function $g^{(2)}_{HS}(\mathbf{r}_1, \mathbf{r}_2)$, that is closely related to the first. While we discuss these functions in terms of their place within the SAFT free energy, they and their conceptual basics are also applicable to other Classical DFT.

The first three terms in the SAFT free energy, F_{ideal} and $F_{hard\ sphere}$, describe the hard-sphere reference system. The F_{ideal} is ubiquitous, and describes particles that have no interactions between them. While the $F_{hard\ sphere}$ term does treat particle interactions, it is so large that it cannot be treated perturbatively, so it is used as a reference term and is incorporated into many very different functionals. I will discuss it more thoroughly in Section 3.4, but I'll state briefly that it is defined to describe a potential between particles that is everywhere zero, except at a distance of one diameter or less, for which the potential becomes infinite. Section 3.4 gives a detailed introduction to the particular functional that we use for the $F_{hard\ sphere}$ term below (that of the White Bear free energy), because while we don't actually modify it in our implementation of inhomogeneous SAFT, we do draw heavily from its ideas when creating our functions. The rest of the terms in $\mathcal{F}$ address different types of attractions between particles. SAFT itself departs from other theories in these last three terms. Each of these terms is itself a functional of the density profile.

The first term in the SAFT functional is the ideal free energy term F_{ideal}, which treats a system of particles that do not interact with each other. This is an obvious

place to start if one is to build the description of particle interaction terms upon a reference system. Its lack of interaction actually causes this term to be the only one that we can construct exactly, with no approximations. To see why, we observe that a system of non-interacting particles is able to satisfy what is usually called the local density approximation (although we shouldn't call it this here because for non-interacting particles it's not an approximation!). The idea is that the free energy functional can be written as an integral of a completely local function of the density profile:

$$\mathcal{F}_{local\ density}[n(\mathbf{r})] = \int f(n(\mathbf{r}))d\mathbf{r} \tag{3.14}$$

where $f(n(\mathbf{r}))$ is the free energy per unit volume of a homogeneous fluid at a density $n(\mathbf{r})$. In essence, each bit of volume becomes its own thermodynamic system, with a free energy equal to that of a homogeneous density of particles at the same local density, and the free energies from all these bits of volume are added up to get the total. The construction neglects any interaction between the particles, so that any spatial variation in the density will be entirely due to the varying external potential. As an approximation for interacting fluids, it does in fact apply to external potentials that modulate the density slowly over space, much more slowly than correlation lengths. It has thus been used in the past to construct portions of the intrinsic free energy functionals beyond the reference F_{ideal} term. It breaks down rather quickly, however, near hard walls for interacting systems, where often the spheres will stack up in 'layers' and the local densities become greater than

bulk freezing densities.

However, F_{ideal} can be constructed exactly in this local density form, so all we need to do is integrate the free energy of an ideal homogeneous system at the local density. Going back to basic thermodynamics and statistical mechanics, we have:

$$F = -k_B T \ln Q_N = -k_B T \ln \left(\frac{V^N}{N! \Lambda^{3N}} \right) \tag{3.15}$$

where Q_N is the ordinary canonical partition function and Λ is the de Broglie thermal wavelength, $\Lambda = \left(\frac{2\pi\beta h^2}{m} \right)^{1/2}$. Using the Stirling approximation for $N!$, we have

$$F^{id} = N k_B T (\ln \Lambda^3 n - 1) \tag{3.16}$$

Taking this as the free energy divided by volume and integrating, we have

$$F_{ideal}[n] = \frac{1}{\beta} \int d\mathbf{r} n(\mathbf{r}) (\ln(\Lambda^3 n(\mathbf{r})) - 1) \tag{3.17}$$

This will be the reference F_{ideal} term, which is commonly used in Classical Density Functional Theory.

3.3 Virial Equation, Mayer functions, and the Carnahan Starling Equation

The second term in the SAFT intrinsic free energy functional, $F_{hard\ sphere}$, is also part of the reference system. The specific hard sphere free energy functional that we use for this term is widely used in the field. I'll introduce the functional and the theory behind it in some detail in Section 3.4 because it is so widely used and, more importantly, because an understanding of the ideas involved is necessary for an understanding of our own work. Before describing the term itself, however, I'll explain in this section some important things that lead up to this theory, namely the Virial equation, Mayer functions, and the Carnahan Starling Equation.

The Virial Equation applies to homogeneous fluids. It equates a thermodynamic, intensive quantity (likes the pressure) to an expansion of the homogeneous density n of the fluid. Its standard form is

$$\frac{\beta P}{n} = 1 + \sum_{i=1}^{\infty} \beta_i \eta^i. \tag{3.18}$$

where

$$\eta \equiv \frac{\pi n \sigma^3}{6} \tag{3.19}$$

is the 'packing fraction'. Here σ is the diameter of the spherical particles of the fluid. The packing fraction is really just a more convenient way to refer to the density, where we give each particle the volume of a sphere and think in terms

of how much of the volume is occupied by particles. We use this dimensionless measure of density extensively throughout our work.

The expansion of Eq. 3.18 comes out of a formulation of the partition function that is most often expressed as a series of diagrams that have well defined rules of construction. A single term (or diagram) in this expansion of the partition function is in fact a spatial integral of particle densities multiplied by a number of what are called Mayer Functions. The derivation starts with the partition function,

$$\Xi = \sum_{N=0}^{\infty} \frac{\exp(N\beta\mu)}{h^{3N}N!} \int ... \int \exp(-\beta\mathcal{H}) d\mathbf{r}^N d\mathbf{p}^N \tag{3.20}$$

$$= \sum_{N=0}^{\infty} \frac{\exp(N\beta\mu)}{h^{3N}N!} \int ... \int \exp(-\beta(V_N + K_N + \sum_i \phi(\mathbf{r}_i)) d\mathbf{r}^N d\mathbf{p}^N \tag{3.21}$$

where V_N is the interaction potential between all the particles in the system, K_N is the total kinetic energy, and $\phi(\mathbf{r})$ is the external potential. If the the interaction potential can be written as a summation of pairwise superimposable interactions, i.e.

$$V_N = \sum_{i<j}^{all\ particles} v(\mathbf{r}_i, \mathbf{r}_j) \tag{3.22}$$

than the partition function can be written as

$$\Xi = \sum_{N=0}^{\infty} \frac{1}{N!} \int ... \int \left(\prod_{i<j}^{N} (1 + f(\mathbf{r}_i, \mathbf{r}_j)) \right) \left(\prod_{i=1}^{N} \frac{\exp(\beta(\mu - \phi(\mathbf{r})))}{\Lambda^3} \right) d\mathbf{r}^N \tag{3.23}$$

where $f(\mathbf{r}_i, \mathbf{r}_j) = \exp(-\beta v(\mathbf{r}_i, \mathbf{r}_j)) - 1$ is the Mayer function between two particles.

Because the $f(\mathbf{r}_i, \mathbf{r}_j)$ are small, we can expand Ξ as a power series in the $f(\mathbf{r}_i, \mathbf{r}_j)$. The diagrams mentioned above aid in keeping track of terms in the expansion and taking the logarithm of Ξ. One of the results is an equation of the form

$$\frac{\beta P}{\rho} = 1 + \sum_{i=1}^{\infty} \beta_i \eta^i \tag{3.24}$$

where the β_i are explicit functions of the $f(\mathbf{r}_i, \mathbf{r}_j)$.

The virial formulation of thermodynamic properties is useful, but it requires an expansion of coefficients, which can be a nuisance computationally, particularly since it tends to converge only slowly. Carnahan and Starling [49, 50] were able to develop a rule for coefficient generation that give approximations to the β_i, but that results in integers that one can use to make a geometric series. Written in its analytic form, this series is a simple, easy to use, and accurate approximation of the pressure in a homogeneous hard-sphere fluid as a function of density (or packing fraction η):

$$\frac{\beta P}{n} = \frac{1 + \eta + \eta^2 - \eta^3}{(1 - \eta)^3} \tag{3.25}$$

Integrating this pressure yields the excess free energy:

$$\frac{\beta F^{ex}}{N} = \frac{\eta(4 - 3\eta)}{(1 - \eta)^2}. \tag{3.26}$$

This equation is specifically very successful in predicting the pressure of the ho-

mogeneous hard sphere fluid at different densities.

3.4 $F_{hard\ sphere}$, Fundamental Measure Theory, and White Bear

We now return to analyzing the terms that make up the SAFT free energy:

$$\mathcal{F}_{SAFT} = F_{ideal} + F_{hard\ sphere} + F_{association} + F_{chain} + F_{dispersion}. \tag{3.27}$$

Remember that the F_{ideal} term treats particles that do not interact with one another. In fact, this one term addresses any aspect of the system that is non-interactive, in the sense that every other term in $\mathcal{F}_{SAFT}$ specifically deals with a different type of potential interaction among the particles. Thus, F_{ideal} is in a sense the most basic reference term in the system. However, when using perturbation theory, the second term, $F_{hard\ sphere}$, which I will describe here, is also treated as part of the reference system, because it is large and cannot be treated as a small perturbation.

The potential interaction it describes is based on the fact that every atom has at its core a 'hard-core' repulsion to any other atom. In other words, as two particles approach each other in space, there is a sudden, sharp spike in potential energy that prevents the two particles from 'overlapping'. The forces here can be complicated, deriving from electrostatics and the exclusion principle, but our classical theories seek to approximate these in simple ways.

The hard sphere potential interaction is characterized by an impenetrable

spherical volume that is centered at a particle's position. The potential between two of these hard spheres discontinuously jumps from zero to infinity when the spheres are a distance apart that is equal to their combined radii:

$$v(r) = \infty, \quad r < r_A + r_B \tag{3.28}$$

$$= 0, \quad r > r_A + r_B \tag{3.29}$$

where r is the distance between the two particles, and r_A and r_B are the radii of the two particles. This hard sphere potential that we use is not the only commonly used method for treating the hard-core repulsion between particles. The Leonard-Jones potential, for example, another widely used potential energy description, approximates the repulsion with a positive term proportional to $\frac{1}{r^{12}}$. However, analytic and continuum theories of liquids are most commonly based on the hard-sphere reference system.

After deciding upon this form for the potential, one must turn to the much more difficult step of designing an appropriate free energy functional. One of the first methods by which people attempted to deal with these interactions, which is actually not limited to hard spheres, was to modify the form of the local density approximation free energy discussed above,

$$F[n] = \int f(n(\mathbf{r}))d\mathbf{r} \tag{3.30}$$

to incorporate information about the particle densities immediately surrounding

each point. They did this by redefining the density at each point to be a convolution of the surrounding density with a weighting function:

$$\bar{n}(\mathbf{r}) = \int w(|\mathbf{r} - \mathbf{r}'|) n(\mathbf{r}') d\mathbf{r}' \tag{3.31}$$

and then using a function of this weighted density as a weighting function in the local density approximation formulation of the free energy:

$$\mathcal{F}_{WDA}[n] = \int \frac{f^{ex}(\bar{n}(\mathbf{r}))}{\bar{n}(\mathbf{r})} n(\mathbf{r}) d\mathbf{r} \tag{3.32}$$

Eq. 3.31 allows one to shape the nature of the interaction indirectly, by changing the structure of the weighting function. For example, if one were to choose for the weighting function the step function $\Theta(|\mathbf{r} - \mathbf{r}'|)$, than the modified density would incorporate in an equal way all the density within a sphere surrounding the particle. A functional constructed in this way would be an oversimplified example of a 'Weighted Density Approximation' (WDA). WDA theories become very complicated, and will often include a weighted function that is itself a function of the density [51].

Fundamental Measure Theory (FMT), created by Rosenfeld in 1989 [52, 53], also defines the free energy in terms of a series of convolutions of densities, but it is a considerable departure from the weighted density approximation theories. It is based on an involved derivation worked out by Perkus and Yevick of an equation of state for the homogeneous hard-sphere fluid. Like the derivation of the Virial Expansion and Carnahan-Starling Equation discussed above, this derivation also

dealt with correlation functions and ultimately expressed thermodynamic properties in terms of homogeneous density. Rosenfeld compared this theory with the derivations of another theory call Scaled Particle Theory, which has to do conceptually with a system of spheres and a growing cavity in which they are not allowed to go. He recognized that the density portion of the Perkis-Yevick equations can be reformulated in terms of densities and functions constructed to describe the geometric properties of spheres. Rosenfeld then discovered that for inhomogeneous systems, he could write down the intrinsic free energy in terms of convolutions of densities with these spherical functions in such a way that the Perkus-Yevick correlation equations were reproduced in the limit of homogeneous density. For the derivation of this functional, which is not directly related to our research, see Rosenfeld's original publication [52], or alternatively see the derivation of Tarazona and Rosenfeld [54–57], which gets to the same functional through different means.

The result of all this is an intrinsic free energy which has the form:

$$\mathcal{F}_{hard\ sphere}[n] = \int \Phi(n_i(\mathbf{r}))d\mathbf{r} \tag{3.33}$$

The integrand Φ here is a local function of $n_i(\mathbf{r})$, which are the convolutions of density with weighting functions that are geometrically related to spheres. In FMT the weighted densities are referred to as 'fundamental measures'. They are defined

as:

$$n_3(\mathbf{r}) = \int n(\mathbf{r}')\Theta(\sigma/2 - |\mathbf{r} - \mathbf{r}'|)d\mathbf{r}' \tag{3.34}$$

$$n_2(\mathbf{r}) = \int n(\mathbf{r}')\delta(\sigma/2 - |\mathbf{r} - \mathbf{r}'|)d\mathbf{r}' \tag{3.35}$$

$$\mathbf{n}_{2V}(\mathbf{r}) = \int n(\mathbf{r}')\delta(\sigma/2 - |\mathbf{r} - \mathbf{r}'|)\frac{\mathbf{r} - \mathbf{r}'}{|\mathbf{r} - \mathbf{r}'|}d\mathbf{r}' \tag{3.36}$$

$$\mathbf{n}_{V1} = \frac{\mathbf{n}_{V2}}{2\pi\sigma}, \quad n_1 = \frac{n_2}{2\pi\sigma}, \quad n_0 = \frac{n_2}{\pi\sigma^2} \tag{3.37}$$

where σ is the hard-sphere diameter.

We can see the spherical nature of the theory by inspecting the n_i. The $n_3(\mathbf{r})$ weighting function is a step function that is designed so that the density is integrated over the volume of a sphere of diameter σ, but will make no contributions outside of this sphere. n_2 only allows for integration of densities on the surface of a sphere, but incorporates no density within or outside of it. $\mathbf{n}_{2V}$ is a vector version of n_2 and is also the gradient of n_3. The others are different versions of the same, modified to have different units.

The form of $\Phi(n_i(\mathbf{r}))$ is restricted to a certain extent by dimensional analysis (the units of each term have to be right!) throughout the derivation, but even given this constraint the theory allows for a certain amount of freedom in its design. Since his derivation of FMT was originally based on concepts in the Perkus-Yevick derivation of the equation of state, Rosenfeld constructed the form of his functional so that in the limit of homogeneous density, the free energy of the system

approaches that given by the Perkus-Yevick equation of state.

While the theory has been a resounding success [52, 53, 58], the use of the Perkus-Yevick equation of state as the underlying, homogeneous limit equation causes problems. The construction of FMT obeys a theorem called the 'contact value theorem,' which states that the pressure at a wall is equal to the temperature multiplied by the density in contact with that wall, $p = kTn_{contact}$. This theorem is very important in our own work, so I'll discuss it in detail below. I mention it here though because for the hard sphere fluid, the Perkus-Yevick equation predicts a pressure that is too high as the bulk freezing density are approached. It consequently overestimates the density at contact at these temperatures. This is problematic, since much of the reason we use classical density functional theory in analyzing inhomogeneous fluids in the first place is to estimate what happens at walls!

In 2002 Roth *et* al. addressed this issue in their version of FMT which they named 'White Bear' [59, 60], anecdotally after a pub that they frequented while developing the theory. They keep the same general form of Rosenfeld's FMT but adjust it so that in the limit of homogeneous density the free energy approaches that of the Mansoori-Carnahan-Starling-Leland equation, a modified version of the Carnahan-Starling equation of state, which we discussed above and which we use directly in our own work. The Carnahan-Starling equation is more accurate at high density than the Perkus-Yevick, so the White Bear hard-sphere free energy functional, $F_{hard\ sphere}$, is overall a more accurate one. It is therefore the hard sphere free energy reference system that we choose to use in our own work.

Below is the entire energy functional written in terms of the fundamental measures, $n_i(\mathbf{r})$:

$$F_{hard\ sphere}[n] = k_B T \int \left(\Phi_1(\mathbf{r}) + \Phi_2(\mathbf{r}) + \Phi_3(\mathbf{r})\right) d\mathbf{r}\ , \tag{3.38}$$

with integrands

$$\Phi_1 = -n_0 \ln\left(1 - n_3\right) \tag{3.39}$$

$$\Phi_2 = \frac{n_1 n_2 - \mathbf{n}_{V1} \cdot \mathbf{n}_{V2}}{1 - n_3} \tag{3.40}$$

$$\Phi_3 = (n_2^3 - 3 n_2 \mathbf{n}_{V2} \cdot \mathbf{n}_{V2}) \frac{n_3 + (1 - n_3)^2 \ln(1 - n_3)}{36\pi n_3^2 \left(1 - n_3\right)^2}, \tag{3.41}$$

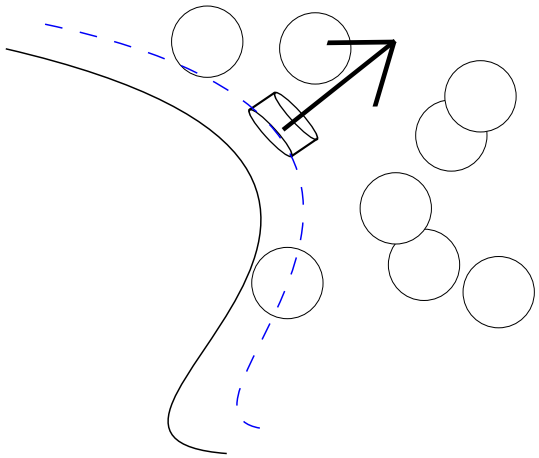

Figure 3.1: A cartoon of our hypothetical system. The wall of the system is either flat or includes a small protrusion that juts out into the volume.

3.5 Contact Value Theorem

The contact value theorem is used directly in our own work and a conceptual understanding of its origin will aid in the conceptual understanding of the functions that we've created. A derivation of it is both justified and sort of awesome, so I dedicate this section to it.

We start by considering a thermodynamic system of a fixed number of particles in contact with a hard wall of arbitrary shape. The thermodynamic equations are:

$$F = U - TS \tag{3.42}$$

$$dU = TdS - pdV \tag{3.43}$$

$$dF = dU - TdS - SdT = -SdT - pdV. \tag{3.44}$$

The volume of our system will be fixed except for a tiny (infinitesimally small) protrusion into it, jutting out from the wall, illustrated in Figure 3.1. We will allow the protrusion to either stick out or not, allowing the wall to either be flat and smooth there or protruding. We'll call the free energy in the two different scenarios F_{flat} and F_{out}, and investigate the difference between them, or in other words what happens as the system loses the bit of volume, dV. The partition functions for these scenarios are

$$Z_{flat} = \int_V ... \int_V \exp(-\phi\{\mathbf{r}^N\}) d\mathbf{r}^N \tag{3.45}$$

$$Z_{out} = \int_{V-dV} ... \int_{V-dV} \exp(-\phi\{\mathbf{r}^N\}) d\mathbf{r}^N \tag{3.46}$$

where $\phi(\{\mathbf{r}^N\})$ is the interaction energy between all the particles and where we have ignored the kinetic energy terms and momentum integrals, since in both systems, which are at the same temperature, these will be the same, and will later cancel out. We would like to write Z_{flat} in terms of Z_{out}, so we'll spatially break up the Z_{flat} integral. The first term will integrate over the same volume as Z_{out}. The next set of terms will treat the integration for one particle within the bit of volume, interacting with all the other particles outside of the volume. The terms after that will integrate for two of the particles within the bit of volume and all the remaining particles in the rest of the volume. The series will continue on in

this fashion, with three particles in the volume, then four, etc.:

$$
\begin{aligned}
Z_{flat} = & \int_{V-dV} ... \int_{V-dV} \exp(-\phi\{\mathbf{r}^N\}) d\mathbf{r}^N \\
& + \int_{V-dV} ... \int_{V-dV} \int_{dV} \exp(-\phi\{\mathbf{r}^N\}) d\mathbf{r}^N \qquad (3.47) \\
& + \int_{V-dV} ... \int_{dV} \int_{V-dV} \exp(-\phi\{\mathbf{r}^N\}) d\mathbf{r}^N ... \\
& + \int_{V-dV} ... \int_{V-dV} \int_{dV} \int_{dV} \exp(-\phi\{\mathbf{r}^N\}) d\mathbf{r}^N \qquad (3.48) \\
& + \int_{V-dV} ... \int_{dV} \int_{V-dV} \int_{dV} \exp(-\phi\{\mathbf{r}^N\}) d\mathbf{r}^N ... \qquad (3.49)
\end{aligned}
$$

The term on the first line is just Z_{out}. Looking at the next set of terms, because every particle is identical it doesn't matter which of them is within the little bit of volume. Every one of these terms will be the same, so they can be replaced by one of them multiplied by N. We will throw away the terms that are of higher order in dV, and there are two arguments that allow us to do this. The simplest one is that dV is small, and so terms with two dVs multiplied together will be smaller. One must be careful with this, however, because the integration is really of the boltzmann factor over these volumes. If the interaction potential between the particles is constructed so that they are highly attracted to each other, then a state in which there are two particles in the bit of volume may have the same order of magnitude probability as the one in which there is just one. In this case we would not be able to say for certain that these terms are so much smaller than the order one dV terms that we could reasonably ignore them. Thus the validity of the derivation depends upon the size of the smallest measurement one can make along

the wall, and the nature of the attractive potential between the particles. In our case and for physically reasonable interactions we deal with an interaction between hard spheres, which exclude other spheres from being too close to them. Thus it's reasonable for us to imagine, given that dV is an arbitrarily small volume, that if there is one hard sphere in the bit of volume, then there is only the one, and any terms that address the situation in which there are two in the bit of volume can be ignored. After applying these arguments we have:

$$Z_{flat} = Z_{out} + N \int_{V-dV} ... \int_{V-dV} \int_{dV} \exp(-\phi(\{\mathbf{r}^N\}))d\mathbf{r}^N \tag{3.50}$$

Now we consider the statistical mechanical definition of the particle density,

$$n(\mathbf{r}) = \frac{N \int_V ... \int_V \exp(-\phi(\{\mathbf{r}^N\}))d\mathbf{r}^{N-1}}{Z_{flat}} \tag{3.51}$$

which is the sum of the boltzmann factors of all the states for which a particle is at position $\mathbf{r}$, divided by the partition function for the system. Comparing this with the right-most term in the Eq. 3.50 we see that:

$$N \int_{V-dV} ... \int_{V-dV} \int_{dV} \exp(-\phi\{\mathbf{r}^N\})d\mathbf{r}^N = Z_{flat} \int_{dV} n(\mathbf{r})d\mathbf{r} \tag{3.52}$$

$$\approx Z_{flat} n(\mathbf{r})dV \tag{3.53}$$

where we make the approximation that because the volume is arbitrarily small

$n(\mathbf{r})$ is constant over it. Thus we have

$$Z_{flat} = Z_{out} + Z_{flat} n(\mathbf{r}) dV \tag{3.54}$$

$$Z_{out} = Z_{flat}(1 - n(\mathbf{r})dV) \tag{3.55}$$

Now we'll consider the change in the free energy when the system goes from one in which a tiny protrusion sticks out from the wall, to one in which the wall is flat, so that the dV during the change will be positive:

$$\begin{aligned} dF = F_{flat} - F_{out} &= -kT \ln(Z_{flat}) + kT \ln(Z_{out}) \\ &= kT \ln\left(\frac{Z_{flat}(1 - n(\mathbf{r})dV)}{Z_{flat}}\right) \\ &= kT \ln\left(1 - n(\mathbf{r})dV\right) \\ &= -kTn(\mathbf{r})dV \end{aligned} \tag{3.56}$$

Then relating this back to thermodynamics:

$$dF = -pdV = -kTn(\mathbf{r})dV \tag{3.57}$$

$$p = kTn(\mathbf{r}) \tag{3.58}$$

Eq. 3.58 is the standard formulation of the contact value theorem. It tells us that the pressure on a hard wall is directly proportional to the density of the particles that are in contact with it.

3.6 Remaining terms in SAFT

Going back to the terms in the overall SAFT free energy functional,

$$\mathcal{F}_{SAFT} = F_{ideal} + F_{hard\ sphere} + F_{association} + F_{chain} + F_{dispersion} \tag{3.59}$$

we come to the last three terms. These terms describe attractive interactions, and are the focus of Chapters 4, 5, and 6. Instead of discussing them all here, I'll describe them in the context of those chapters.

3.7 The convolution theorem

Lastly within this introduction I will introduce a theorem, the convolution theorem, that is of practical importance to the rest of this text. This theorem motivates our preference of using density convolutions within our functionals.

One of the largest advantages to using Fundamental Measure Theory, and one that may not be immediately obvious, is that the convolutions that combine to construct this functional allow for very efficient computation. For an example, let's look at a free energy term,

$$F = \iint n(\mathbf{r}_1)n(\mathbf{r}_2)w(|\mathbf{r}_1 - \mathbf{r}_2|)d\mathbf{r}_1 d\mathbf{r}_2, \tag{3.60}$$

in which particles interact according to the weighting function w, which depends on the distance between two particles. The White Bear free energy is composed of integrals similar to this. It may seem at first glance that the size of the computational calculation of this double integral would scale as N^2, where N is the number of grid points in the system. It is true that in the case of FMT, the weighting functions cut off the integrals at a size on the order of a sphere of particle radius, but this can still be a large enough volume so that a double integral for which one of the volumes is this size and the other is the size of the whole system is likely be too costly for practical computation. FMT is saved, however, by what is called the convolution theorem, combined with the Fast Fourier Transform algorithm. The convolution theorem states that when one takes the Fourier transform of a spatial convolution of two functions, the result in k-space is simply the product of the two

functions:

$$h(\mathbf{x}) = (f * g)(\mathbf{x}) = \int f(\mathbf{y})g(\mathbf{x}-\mathbf{y})d\mathbf{y} \tag{3.61}$$

$$\hat{h}(\mathbf{k}) = \hat{f}(\mathbf{k})\hat{g}(\mathbf{k}) \tag{3.62}$$

The Fast Fourier Transform algorithm allows one to take Fourier transforms for a complete range of wave vectors $\mathbf{k}$ at a cost of $N \ln N$, as opposed to N^2, even though it may seem that a separate integral at every value of $\mathbf{k}$ would be necessary. Writing Eq 3.60 as

$$F = \int n(\mathbf{r}_1)\bar{n}(\mathbf{r}_1)d\mathbf{r}_1 \tag{3.63}$$

$$\bar{n}(\mathbf{r}_1) = \int n(\mathbf{r}_2)w(|\mathbf{r}_1 - \mathbf{r}_2|)d\mathbf{r}_2 \tag{3.64}$$

The convolution theorem allows us to state that

$$\hat{\bar{n}}(\mathbf{k}) = \hat{n}(\mathbf{k})\hat{w}(\mathbf{k}) \tag{3.65}$$

So if we take the Fourier transforms of $n(\mathbf{r})$ and $w(\mathbf{r})$ for all $\mathbf{k}$ values (which computationally scales as $N \ln N$), multiply to get $\hat{\bar{n}}$, and then take the Fourier transform of $\hat{\bar{n}}$ to get $\bar{n}$ (which once again scales as $N \ln N$), we can arrive back at

the equation

$$F = \int n(\mathbf{r}_1)\bar{n}(\mathbf{r}_1)d\mathbf{r}_1 \tag{3.66}$$

$$\tag{3.67}$$

having only every taken $N \ln N$ time. This integral can be done in real space (computationally scaling as simply N), and Voila! We're able to perform a double integral in real space in an $N \ln N$ amount of time. For large systems this can certainly be the difference between practically possible and impossible computations. The proof is short and pretty so I'll relate it here.

Say there is a function $h(\mathbf{x})$ such that

$$h(\mathbf{x}) = (f * g)(\mathbf{x}) = \int f(\mathbf{y})g(\mathbf{x}-\mathbf{y})d\mathbf{y} \tag{3.68}$$

The Fourier transforms of the two input functions are

$$\hat{f}(\mathbf{k}) = \int f(\mathbf{y}) \exp(-\mathbf{k}\cdot\mathbf{y})d\mathbf{y} \tag{3.69}$$

$$\hat{g}(\mathbf{k}) = \int g(\mathbf{y}) \exp(-\mathbf{k}\cdot\mathbf{y})d\mathbf{y}. \tag{3.70}$$

and the Fourier transform of h is

$$\hat{h}(\mathbf{k}) = \int h(\mathbf{z}) \exp(-\mathbf{k}\cdot\mathbf{z})d\mathbf{z} = \int \left(\int f(\mathbf{y})g(\mathbf{z}-\mathbf{y})d\mathbf{y} \right) \exp(-\mathbf{k}\cdot\mathbf{z})d\mathbf{z} \tag{3.71}$$

because the two integrals are taken over all space, we can use a change of variables

to

$$\mathbf{x} \equiv \mathbf{z} - \mathbf{y} \tag{3.72}$$

and then reorder the integrals to find

$$\hat{h}(\mathbf{k}) = \int f(\mathbf{y}) \exp(-\mathbf{k} \cdot \mathbf{y}) d\mathbf{y} \int g(\mathbf{x}) \exp(-\mathbf{k} \cdot \mathbf{x}) d\mathbf{x} \tag{3.73}$$

$$= \hat{f}(\mathbf{k}) \hat{g}(\mathbf{k}) \tag{3.74}$$

This concludes the general introduction to the Classical DFT and liquid state concepts that are used throughout my research. The following three chapters describe three of my research projects individually.

4 Contact Distribution Function

4.1 Introduction

In this chapter we discuss our investigation into the value of the distribution function of an inhomogeneous hard-sphere fluid at contact. This is a function that contains information about how densities at two positions, separated by a distance of one diameter so that spheres located at the positions are in contact, are correlated with each other. I will define it in more detail below. It plays a critical role in SAFT, since the ability to accurately estimate contact between spheres dictates the ability to accurately estimate when interaction sites on the surface of those spheres are overlapping, and it's this overlap that dictates how particles interact within the 'chain' and 'association' free energy terms in SAFT. We define two averaged values for the distribution function at contact, and derive formulas for each of them from the White Bear version of the FMT functional, using an assumption of thermodynamic consistency. We have tested these formulas, as well as two existing formulas against Monte Carlo simulations, and have found excellent agreement between the Monte Carlo data and one of our averaged distribution functions.

A key input to the SAFT free energy functionals is the distribution function evaluated at contact, which is identical to the contact value of the cavity correlation function for hard spheres, and is required for the association term in the SAFT free energy, and as well for a term labeled the 'chain' term, which is used in SAFT

free energy functionals for polymers.

Yu and Wu introduced in 2002 a functional for the association term of the free energy, which included a functional for the contact value of the distribution function (described in Section 4.3.5) [4], which has subsequently been used in the development of other SAFT-based functionals [61, 62]. Also, two functionals for the chain term have recently been introduced, one which uses the distribution function of Yu and Wu [62] and another which introduces a new approximation for the contact value of the distribution function [3]. Here we will briefly describe how the contact value of the distribution function has been used in two of these recent papers introducing SAFT-based classical density functionals. For simplicity, we will use our own notation to describe the work of these authors.

In his paper presenting a density functional based on the PCP-SAFT equation of state [3], Gross introduces the chain free energy in SAFT as

$$\frac{F_{chain}}{kT} = -(m-1)\int n(\mathbf{r})\left(\ln\left(n_A(\mathbf{r})g_\sigma^A(\mathbf{r})\right)-1\right)d\mathbf{r} \tag{4.1}$$

where $n_A(\mathbf{r})$ is a weighted density defined as

$$n_A(\mathbf{r}) = \int n(\mathbf{r}')\frac{\delta(\sigma-|\mathbf{r}-\mathbf{r}'|)}{4\pi\sigma^2}d\mathbf{r}' \tag{4.2}$$

and $g_\sigma^A(\mathbf{r})$ is the local value of the distribution function at contact, which we define

as

$$g_\sigma^A(\mathbf{r}) = \frac{1}{n(\mathbf{r})n_A(\mathbf{r})} \int n^{(2)}(\mathbf{r}, \mathbf{r}+\mathbf{r}') \frac{\delta(\sigma - |\mathbf{r}'|)}{4\pi\sigma^2} d\mathbf{r}' \tag{4.3}$$

In Section 4.3.4 we describe Gross's approximation for this function.

In a paper describing a classical density functional for inhomogeneous associating fluids [4], Yu and Wu define the association free energy as

$$\frac{F_{assoc}}{kT} = \sum_i \int \zeta(\mathbf{r}) n_0(\mathbf{r}) \left(\ln X_i(\mathbf{r}) - \frac{1}{2} X_i(\mathbf{r}) + \frac{1}{2} \right) d\mathbf{r} \tag{4.4}$$

$$X_i(\mathbf{r}) = \frac{1}{1 + \sum_j \frac{n_0(\mathbf{r}) g_\sigma^S(\mathbf{r})}{\zeta(\mathbf{r})} X_j(\mathbf{r}) \kappa_{ij} \left(e^{\beta\epsilon_{ij}} - 1 \right)}. \tag{4.5}$$

where $X_i(\mathbf{r})$ is the fraction of interaction sites of type i at position $\mathbf{r}$ that are unoccupied, $n_0(\mathbf{r})$ is a weighted density defined in Equation 4.8, $\zeta(\mathbf{r})$ is a nonlocal measure of the density gradient defined in Equation 4.27 and discussed in Section 3.4, and $g_\sigma^S(\mathbf{r})$ is a form of the distribution function at contact, which we define in Equation 4.7. In Section 4.3.5 I present the approximation to $g_\sigma^S(\mathbf{r})$ introduced by Yu and Wu. Given these differing approaches, it seems valuable to examine this property of the hard-sphere fluid through direct simulation, in order to establish the advantages and disadvantages of each approach.

Although these recent works have introduced approximate functionals for the contact value of the distribution function for an inhomogeneous hard-sphere fluid [3,4], there had not been a study that specifically addressed this functional. In our work we introduced two definitions for the locally averaged distribution function of

an inhomogeneous system. Given these definitions, I'll present a thermodynamic derivation for each distribution function from the free energy functional. We will then discuss the distribution functions of Yu and Wu and of Gross, and will end by comparing all four approximations with Monte-Carlo simulations of the hard-sphere fluid at a variety of hard-wall surfaces.

4.2 Distribution function with inhomogeneity

We define our terms using the two-particle density $n^{(2)}(\mathbf{r}_1, \mathbf{r}_2)$, which gives the probability per unit volume squared of finding one particle at position $\mathbf{r}_1$ and the other at position $\mathbf{r}_2$. The pair distribution function is defined in terms of the pair density (See Eq 3.2):

$$g(\mathbf{r}_1, \mathbf{r}_2) \equiv \frac{n^{(2)}(\mathbf{r}_1, \mathbf{r}_2)}{n(\mathbf{r}_1)n(\mathbf{r}_2)} \tag{4.6}$$

In a homogeneous fluid, the pair distribution only depends on the distance $|\mathbf{r}_1 - \mathbf{r}_2|$ and can be expressed as a function of a single variable, and the contact value of the distribution function is its value when evaluated at a distance of the diameter σ. The pair distribution function of an *inhomogeneous* fluid is not as simple, but it is desirable for reasons of computational efficiency to construct classical density functionals using only one-center convolutions. Moreover, a local function is helpful when defining functionals based on perturbation theory, such as those in Equations 4.1-5.6. This leads us to seek a *local* value for g_σ that is dependent upon

only one position variable $\mathbf{r}$. There are two reasonable options for defining such a local function: a symmetric formulation such as that used in Equation 4.4 (which we refer to as S) and an asymmetric formulation such as that used in Equation 4.1 (which we refer to as A).

For the symmetric S case, the distribution function at contact is given by:

$$g_\sigma^S(\mathbf{r}) \equiv \frac{1}{n_0(\mathbf{r})^2} \int n^{(2)}(\mathbf{r}-\mathbf{r}', \mathbf{r}+\mathbf{r}') \frac{\delta(\sigma/2 - |\mathbf{r}'|)}{\pi\sigma^2} d\mathbf{r}' \tag{4.7}$$

where σ is the hard sphere diameter and the density n_0 is one of the fundamental measures of Fundamental Measure Theory (FMT). The functional $g_\sigma^S(\mathbf{r})$ is defined to treat the geometrically symmetric possibility of spheres touching at the position $\mathbf{r}$ as illustrated in Figure 4.1.

$$n_0(\mathbf{r}) = \int n(\mathbf{r}') \frac{\delta(\sigma/2 - |\mathbf{r}-\mathbf{r}'|)}{\pi\sigma^2} d\mathbf{r}' \tag{4.8}$$

This functional $n_0(\mathbf{r})$ gives a density averaged over all spheres that touch at the position $\mathbf{r}$. Together, $n_0(\mathbf{r})$ and $g_\sigma^S(\mathbf{r})$ are used in the association free energy given in Equations 4.4-4.5.

In contrast, the asymmetrically averaged A distribution function is given by

$$g_\sigma^A(\mathbf{r}) \equiv \frac{1}{n(\mathbf{r}) n_A(\mathbf{r})} \int n^{(2)}(\mathbf{r}, \mathbf{r}+\mathbf{r}') \frac{\delta(\sigma - |\mathbf{r}'|)}{4\pi\sigma^2} d\mathbf{r}' \tag{4.9}$$

where the density $n_A(\mathbf{r})$ is analogous to $n_0(\mathbf{r})$, but measures the density of spheres

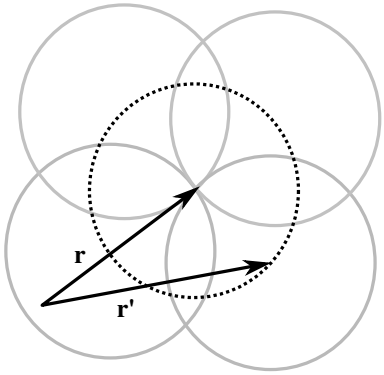

Figure 4.1: Set of hard spheres that are included in $n_0(\mathbf{r})$, which consist of those which just touch the point $\mathbf{r}$.

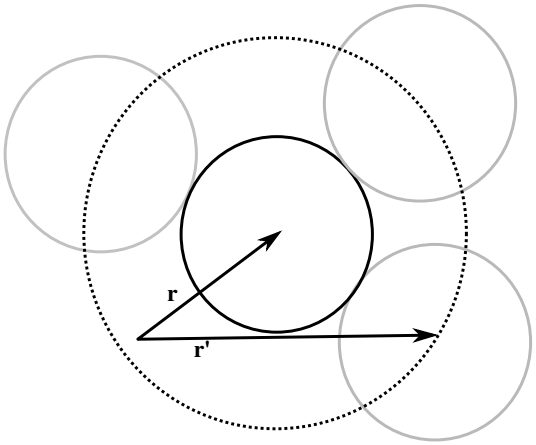

Figure 4.2: Set of hard spheres that are included in $n_A(\mathbf{r})$, which consist of those which just touch a sphere centered at $\mathbf{r}$. The dashed line illustrates the surface over which contact is possible.

that are touching a sphere that is located at point $\mathbf{r}$, as illustrated in Figure 4.2.

$$n_A(\mathbf{r}) = \int n(\mathbf{r}') \frac{\delta(\sigma - |\mathbf{r} - \mathbf{r}'|)}{4\pi\sigma^2} d\mathbf{r}' \tag{4.10}$$

Thus g_σ^A corresponds to an average of the two-particle density over spheres touching a sphere that is located at the position $\mathbf{r}$. The functionals $n_A(\mathbf{r})$ and $g_\sigma^A(\mathbf{r})$ are used in the chain free energy given in Equation 4.1.

4.3 Theoretical Approaches

4.3.1 Homogeneous limit

In order to motivate our derivation of the distribution function at contact for the *inhomogeneous* hard-sphere fluid, we begin by deriving the well-known formula for g_σ for the *homogeneous* fluid that comes from the Carnahan-Starling free energy. The contact value of the distribution function density can be found by using the contact-value theorem, discussed in Chapter 3, which states that the pressure on any hard surface is determined by the density at contact:

$$p_{SAS}(\mathbf{r}_c) = k_B T n(\mathbf{r}_c) \tag{4.11}$$

where $\mathbf{r}_c$ is a position of a sphere that would be in contact with the hard surface, $n(\mathbf{r}_c)$ is the density at this point $\mathbf{r}_c$, and $p_{SAS}(\mathbf{r}_c)$ is the pressure that the spheres exert on the surface at the same point. This pressure is understood as the ratio of

force to an infinitesimal element of *solvent accessible surface* (SAS) area. In the homogeneous fluid, the contact-value theorem implies that

$$p_{SAS} = k_B T n g_\sigma \tag{4.12}$$

where p_{SAS} is the pressure on a hard sphere's solvent accessible surface. This pressure can be readily computed from the dependence of the Carnahan-Starling free energy on hard sphere radius:

$$F_{HS} = N k_B T \frac{4\eta - 3\eta^2}{(1-\eta)^2} \tag{4.13}$$

where $\eta \equiv \frac{\pi}{6}\sigma^3 n$ is the filling fraction. We compute the pressure using the total force with respect to a changing radius of all the spheres. To find the pressure, we divide this force by $4\pi\sigma^2$, which is the SAS area of a single hard sphere, illustrated in Figure 4.2. Finally, we divide by N to account for the total area of all the spheres in the fluid.

$$p_{SAS} = \frac{1}{N 4\pi\sigma^2}\frac{dA_{HS}}{dR} \tag{4.14}$$

$$= \frac{1}{N 4\pi\sigma^2}\frac{1}{2}\frac{dA_{HS}}{d\sigma} \tag{4.15}$$

$$= k_B T n \frac{1 - \frac{\eta}{2}}{(1-\eta)^3} \tag{4.16}$$

Using the contact-value theorem, we thus find the well-known distribution function evaluated at contact.

$$g_\sigma = \frac{1 - \frac{\eta}{2}}{(1-\eta)^3} \tag{4.17}$$

Extending this derivation to the inhomogeneous fluid requires that I find the pressure felt by the surface of particular spheres.

4.3.2 Asymmetrically averaged distribution function

We will begin the derivation of the locally averaged distribution function with the asymmetric definition of $g_\sigma^A(\mathbf{r})$ given in Equation 4.9, which is averaged over contacts in which one of the two spheres is located at position $\mathbf{r}$. This distribution function is related to the contact density averaged over the solvent accessible surface of a sphere located at $\mathbf{r}$, and can thus be determined by finding the pressure on that surface. We find this pressure from the change in free energy resulting from an infinitesimal expansion of spheres located at position $\mathbf{r}$. From this pressure, we derive a formula for the distribution function $g_\sigma^A(\mathbf{r})$ as was done in the previous section:

$$p_{SAS}(\mathbf{r}) = \frac{1}{n(\mathbf{r}) 4\pi\sigma^2} \frac{1}{2} \frac{\delta F_{HS}}{\delta \sigma(\mathbf{r})} \tag{4.18}$$

$$g_\sigma^A(\mathbf{r}) = \frac{1}{n(\mathbf{r}) n_A(\mathbf{r})} \frac{1}{k_B T 4\pi\sigma^2} \frac{1}{2} \frac{\delta F_{HS}}{\delta \sigma(\mathbf{r})} \tag{4.19}$$

where $\sigma(\mathbf{r})$ is the diameter of spheres located at position $\mathbf{r}$. Details regarding the evaluation of the functional derivative $\frac{\delta F_{HS}}{\delta \sigma(\mathbf{r})}$ are discussed in Appendix A. Equation 4.19 is an exact expression for $g_\sigma^A(\mathbf{r})$ as defined in Equation 4.9. However, since we do not know the exact hard-sphere free energy, we approximate F_{HS} using FMT. The equation for g_σ^A found using FMT requires finding convolutions of local derivatives of the free energy, making this formulation computationally somewhat more expensive than the free energy itself.

4.3.3 Symmetrically averaged distribution function

We now address the symmetrically averaged distribution function, which is defined in Equation 4.7. This corresponds to the distribution function averaged for spheres *touching at a given point*. In this case, we conceptually would like to evaluate the pressure felt by the surface of spheres where that surface is located at point $\mathbf{r}$. We can approximate this value by assuming that this pressure will be simply related to the free energy density at point $\mathbf{r}$. Through a process similar to the previous derivations, this leads to the expression

$$g_\sigma^S(\mathbf{r}) = \frac{1}{n_0(\mathbf{r})^2} \frac{1}{4\pi\sigma^2} \frac{1}{2} \frac{\partial \Phi(\mathbf{r})}{\partial \sigma} \tag{4.20}$$

where $\Phi(\mathbf{r}) = \Phi_1(\mathbf{r}) + \Phi_2(\mathbf{r}) + \Phi_3(\mathbf{r})$ is the dimensionless free energy density. This expression is an approximation—unlike the analogous Equation 4.19—because it assumes that there is available a local functional $\Phi(\mathbf{r})$ whose derivative provides

the pressure needed to compute $g_\sigma(\mathbf{r})$. Equation 4.20 requires that we evaluate the derivatives of the fundamental measures $n_\alpha(\mathbf{r})$ with respect to diameter, which leads me to derivatives of the δ function, which we can simplify and approximate using an assumption of a reasonably smooth density:

$$\frac{\partial n_2(\mathbf{r})}{\partial \sigma} = \frac{1}{2}\int \delta'(\frac{\sigma}{2} - |\mathbf{r}-\mathbf{r}'|)n(\mathbf{r}')d\mathbf{r}' \tag{4.21}$$

$$= \frac{2}{\sigma}n_2(\mathbf{r}) - \frac{1}{2}\int \delta\left(\frac{\sigma}{2} - |\mathbf{r}-\mathbf{r}'|\right)\frac{\mathbf{r}-\mathbf{r}'}{|\mathbf{r}-\mathbf{r}'|}\cdot\nabla n(\mathbf{r}')d\mathbf{r}' \tag{4.22}$$

$$\approx \frac{2}{\sigma}n_2(\mathbf{r}) \tag{4.23}$$

In the systems that we study, the density is *not* reasonably smooth, but we can state empirically making this approximation nevertheless improves the predictions of our functional g_σ^S, while at the same time reducing its computational cost by avoiding the need to calculate any additional weighted densities or convolutions.

4.3.4 Gross's asymmetrically averaged distribution functional

One approximation for the distribution function is that of Gross [3], which is of the asymmetrically averaged variety (g_σ^A):

$$g_\sigma^{\text{Gross,A}}(\mathbf{r}) = \frac{1-0.5\bar{\eta}(\mathbf{r})}{(1-\bar{\eta}(\mathbf{r}))^3} \tag{4.24}$$

where $\bar{\eta}$ is defined as

$$\bar{\eta} = \frac{1}{8} \int n(\mathbf{r}')\Theta(\sigma - |\mathbf{r} - \mathbf{r}'|)d\mathbf{r}' \tag{4.25}$$

This formula is arrived at by using the density averaged over all spheres that overlap a point $\mathbf{r}$ in the Carnahan-Starling equation for the distribution function at contact, given in Equation 4.17.

4.3.5 Yu and Wu's symmetrically averaged functional

Yu and Wu developed a functional for the distribution function evaluated at contact which is symmetrically averaged [4]. However, instead of using n_0 as the corresponding density, they use a density given by

$$n_{\mathrm{Yu}}(\mathbf{r}) = n_0(\mathbf{r})\zeta(\mathbf{r}) \tag{4.26}$$

$$\zeta = 1 - \frac{\mathbf{n_2} \cdot \mathbf{n_2}}{n_2^2} \tag{4.27}$$

where the function ζ is a measure of local inhomogeneity at the point of contact, and has the effect of reducing this density at interfaces. Because of this difference, the distribution function of Yu and Wu cannot be directly compared with g_σ^S as defined in Equation 4.7. Therefore in order to make a comparison we move the

factors of ζ in Equation 4.26 from the density into the distribution function itself.

$$g_\sigma^{\mathrm{Yu,S}} = \zeta^2 g_\sigma^{\mathrm{Yu}} \tag{4.28}$$

$$= \zeta^2 \left(\frac{1}{1-n_3} + \frac{1}{4}\frac{\sigma n_2 \zeta}{(1-n_3)^2} + \frac{1}{72}\frac{\sigma^2 n_2^2 \zeta}{(1-n_3)^3} \right) \tag{4.29}$$

where g_σ^{Yu} is the distribution function as defined in reference [4], and $g_\sigma^{\mathrm{Yu,S}}$ is the function we will examine in this paper.

4.4 Comparison with simulation

We performed a Monte-Carlo simulation of the hard sphere fluid to measure the contact value of the distribution function for several simple inhomogeneous configurations. For each configuration, we compute the mean density, and the contact values of the distribution function, averaged as defined in Equations 4.9 and 4.7. We compare these with the four functionals presented in sections 4.3.2 to 4.3.5. We constructed our functionals using both the original White Bear functional [59] as well as the mark II version of the White Bear functional [60], but the results were visually indistinguishable on our plots, so we exclusively show the results due to the original White Bear functional.

We simulate the inhomogeneous hard sphere fluid at four hard-wall interfaces. The first and simplest is a flat hard wall. We then study two convex hard surfaces. One is an excluded sphere with diameter 2σ, which corresponds to a "test particle" simulation with one of a hard sphere at the origin with diameter σ. The second is an

excluded sphere with diameter 6σ, which demonstrates behavior typical of mildly convex hard surfaces. Finally, we study a concave surface given by a hard cavity in which our fluid is free to move up to a diameter of 16σ, which demonstrates behavior typical of mildly concave surfaces. In each case, we performed a low-density (filling fraction 0.1) and high-density (filling fraction 0.4) simulation. We performed additional computations over a wider range of curvatures and densities, but chose these to present as typical examples.

4.4.1 Low density

We begin by presenting our low-density results, corresponding to a filling fraction of 0.1, which are shown in Figure 4.3. At this low density, the contact value of the distribution function in the bulk is only 1.3, indicating that correlations are indeed small and that the fluid should be relatively easy to model. Indeed, the contact density at the hard surface is only around 50% higher than the bulk, and the FMT predicted density is close to indistinguishable from the true density for each of the four configurations, as seen in the bottom subpanel of each subfigure within Figure 4.3.

The g_σ^A distribution function in each configuration (plotted in the top panel of each subfigure within Figure 4.3) is very flat, with only small, smooth changes as the surface is approached. Our functional g_σ^A very closely matches the Monte Carlo predictions in each case, while that of Gross consistently underestimates the distribution at the interface by a significant margin. We note that the theoretical

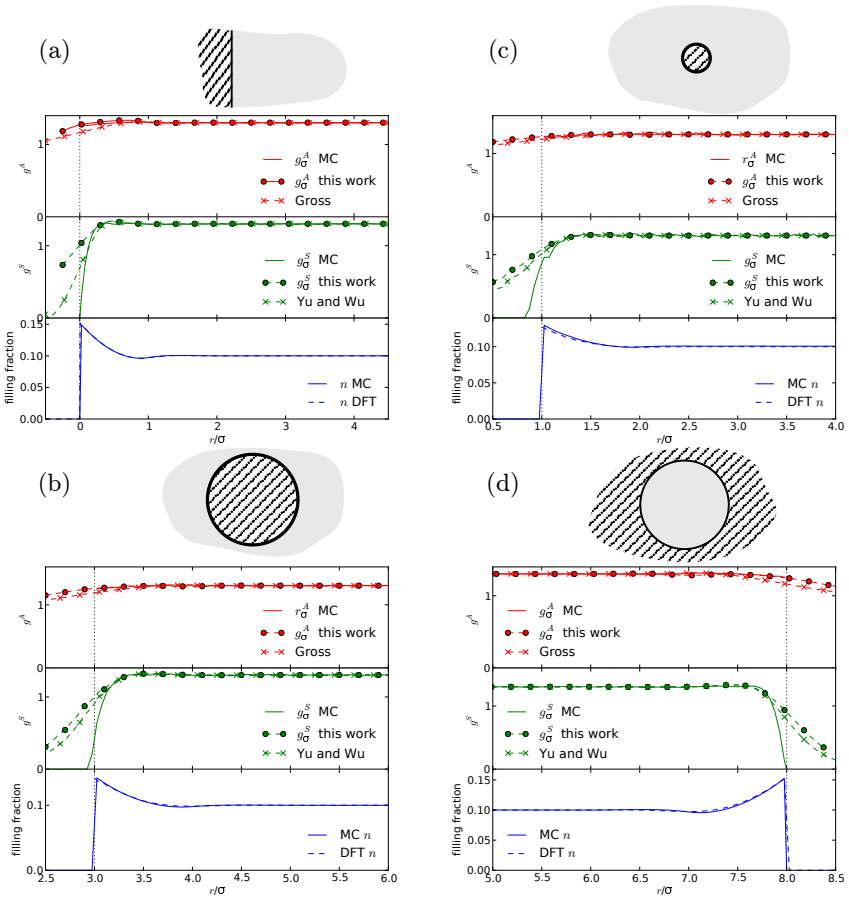

Figure 4.3: Density and distribution function in systems with a "low density" bulk filling fraction of 0.1. The subplots each show a different system: (a) next to a flat hard wall, (b) around a hard sphere with an excluded diameter of 6σ, (c) around a hard sphere with an excluded diameter of 2σ, and (d) within a spherical cavity with an included diameter of 16σ. In the top and middle panels of each subfigure respectively are the asymmetrically averaged distribution function g_σ^A (defined in Equation 4.9) and the symmetrically averaged distribution function g_σ^S (defined in Equation 4.7). The results of Monte Carlo, our functional, and one previously published functional [3,4] are compared in each case. The bottom panels show the density computed with Monte Carlo and with DFT.

curves extend into the region from which the fluid is excluded. This value corresponds to the distribution function that would be observed in the vanishingly unlikely scenario in which there was a sphere present at that location. Naturally, we are unable to observe this quantity in our Monte Carlo simulations.

The g_σ^S distribution function (plotted in the middle panels of Figure 4.3) shows considerably more structure, as well as additional variation due to the curvature of the hard surface. The symmetric distribution function is nonzero at locations where spheres may touch, which for a convex hard surface means that g_σ^S may be nonzero in the volume in which hard spheres are excluded. In every configuration studied, the agreement between the theoretical predictions and the Monte Carlo simulation in each case is very poor in the region where there should be no contacts at all. Because n_0 is comparable to its bulk value in this region, this means that these functionals predict a significant number of contacts in the region where there should be none. The distribution function of Yu and Wu [4] and ours described in Section 4.3.3 give similar results, with slightly larger errors in our prediction.

4.4.2 High density

At a higher density corresponding to a filling fraction of 0.4, correlations are much stronger, with the bulk contact value of the distribution function of 3.7, as seen in Figure 4.4. This results in larger oscillations in the density at the hard surfaces, and correspondingly more interesting behavior in the distribution function near the interface, as shown in the bottom panels of the plots in Figure 4.4. The density

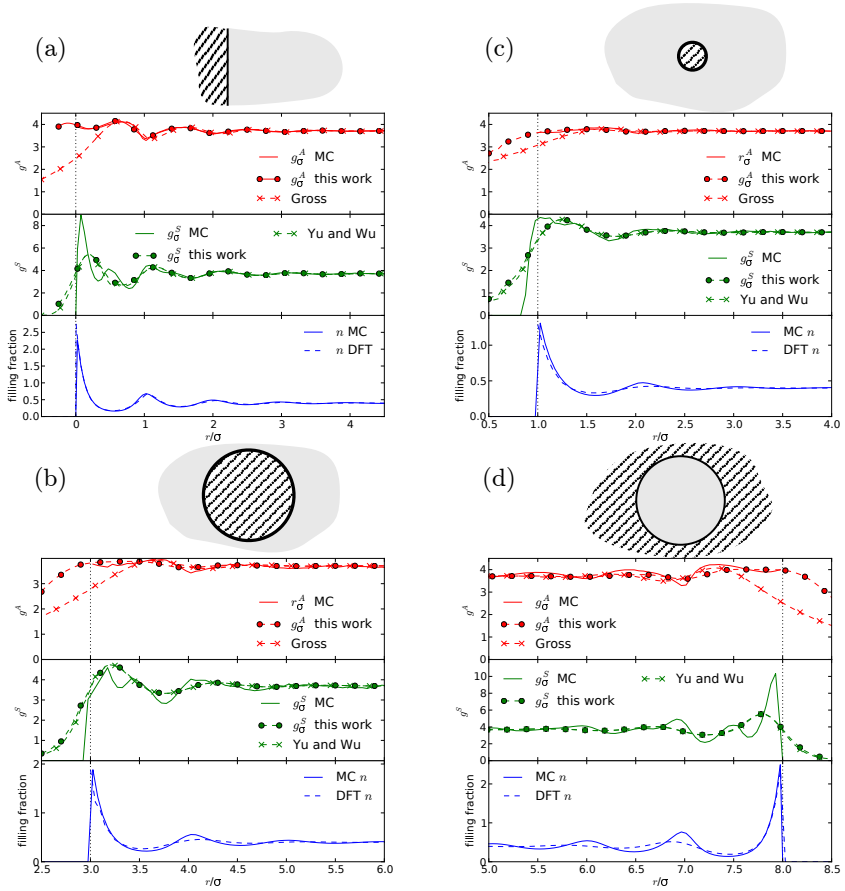

Figure 4.4: Density and distribution function in systems with a "high density" bulk filling fraction of 0.4. The subplots each show a different system: (a) next to a flat hard wall, (b) around a hard sphere with an excluded diameter of 6σ, (c) around a hard sphere with an excluded diameter of 2σ, and (d) within a spherical cavity with an included diameter of 16σ. In the top and middle panels of each subfigure respectively are the asymmetrically averaged distribution function g_σ^A (defined in Equation 4.9) and the symmetrically averaged distribution function g_σ^S (defined in Equation 4.7). The results of Monte Carlo, our functional, and one previously published functional [3,4] are compared in each case. The bottom panels show the density computed with Monte Carlo and with DFT.

predicted by the White Bear functional agrees reasonably well with the simulation results, although not so well as it did at lower density. The discrepancies are largest in the case of the spherical cavity (Figure 4.4d), in which the DFT considerably underestimates the range of the density oscillations.

The asymmetric version of the distribution function (plotted in the top panels of Figure 4.4) once again displays relatively smooth behavior with a few small oscillations near the interface, and a somewhat elevated value within a diameter of the hard surface, with the magnitude of this elevation somewhat different in each configuration. As was the case at low density, our distribution function g_σ^A matches very closely the Monte Carlo data, reproducing quite well the structure near the interface in each configuration, although in the spherical cavity there is a small, but significant discrepancy, comparable to the discrepancy found in the density itself. In each case, the distribution of Gross dramatically underestimates the value at the interface, at one extreme by 40% in the case of the spherical cavity (Figure 4.4d), and at the other extreme by 15% in the test-particle scenario (Figure 4.4c).

The symmetrically averaged distribution function (plotted in the middle panels of Figure 4.4) shows considerably more structure near the interface at high density, and this structure varies considerably depending on the curvature of the hard surface. In each case, this structure is not reflected in the theoretical predictions, neither that of this paper, nor that of Yu and Wu [4]. As was the case at low density, both functionals give significant and finite values in the region in which there are no contacts, but at high density they also miss the large oscillations that

are present near the flat wall and the concave surface (Figures 4.4a and 4.4d). As was the case at low density, the functional of Yu and Wu [4] gives slightly better agreement with the simulation results than that which we derive in Section 4.3.3.

4.5 Conclusion

We investigated several approximations to the contact value of the distribution function for inhomogeneous fluid distributions corresponding to flat, concave, and convex walls. We defined and simulated two averages of the distribution function, an asymmetric A average centered at the location of one of the two spheres that is in contact, and a symmetric S average centered at the point of contact of touching spheres. For each average, we derived a functional form from FMT, and also found an approximation that has been used in the literature. When compared with essentially exact Monte Carlo simulations, the A distribution function derived from Fundamental Measure Theory in Section 4.3.2 gives excellent results for each surface, at both high density and low density. The other three approximations that we studied all showed significant and systematic deviations under some circumstances. Thus, we recommend that creators of SAFT-based classical density functionals consider using the g_σ^A functional defined in Section 4.3.2.

5 Improved Association Term in SAFT Classical DFT for water

5.1 Introduction

In this chapter we present a modification to a SAFT-based classical density functional theory for water that was recently published by my research group [63]. In Chapter 4 we developed and tested a functional for the averaged radial distribution function at contact of the hard-sphere fluid that is dramatically more accurate at interfaces than earlier approximations. We now incorporate this improved functional into the association term of our free energy functional for water, improving its description of hydrogen bonding. We examine the effect of this improvement by studying two hard solutes (a hard hydrophobic rod and a hard sphere) and a Lennard-Jones approximation of a krypton atom solute. The improved functional leads to a moderate change in the density profile and a large decrease in the number of hydrogen bonds broken in the vicinity of the hard solutes. We find an improvement of the partial radial distribution for a krypton atom in water when compared with experiment.

Water, the universal solvent, is of critical practical importance, and a continuum description of water is in high demand for a solvation model. A number of recent attempts to develop improved solvation models for water have built on the approach of classical density functional theory (DFT) [64–70]. There are two general approaches used to construct a classical DFT for water. The first is to choose

a convenient functional form which is then fit to properties of the bulk liquid at a given temperature and pressure [64–71]. Using this approach, it is possible to construct a functional that reproduces the exact second-order response function of the liquid under the fitted conditions. However, this class of functional will be less accurate at other temperatures or pressures—and in the inhomogeneous scenarios in which solvation models are applied. The second approach is to construct a functional by applying liquid-state theory to a model system, and then fit the model to experimental data such as the equation of state [61, 63, 72–80].

The association contribution to the SAFT free energy uses Wertheim's first-order thermodynamic perturbation theory to describe an associating fluid as hard-spheres with strong associative interactions at specific sites on the surface of each sphere [81–84]. These association sites have an attractive interaction at contact, and rely on the hard-sphere pair distribution function at contact g_σ^{HS} in order to determine the extent of association. While this function is known for the homogeneous hard-sphere fluid, it must be approximated for inhomogeneous systems, such as occur at liquid interfaces.

In Chapter 4 we examined the pair distribution function at contact in various inhomogeneous configurations. We tested the accuracy of existing approximations for the pair distribution function at contact [3, 4], and derived a significantly improved approximation for the averaged distribution function at contact. In this chapter we apply this improved g_σ^{HS} to the SAFT-based classical density functional for water developed by Hughes *et al.* [63]. This functional was constructed to reduce in the homogeneous limit to the 4-site optimal SAFT model for water

developed by Clark *et* al. [72]. The DFT of Hughes *et al.* uses the association free energy functional of Yu and Wu [4], which is based on a g_σ^{HS} that we have since found to be inaccurate [85]. In this chapter, we will examine the result of using the improved functional for g_σ^{HS} to construct an association free energy functional.

5.2 Method

The classical density functional for water of Hughes *et al.* consists of four terms:

$$F[n(\mathbf{r})] = F_{\text{ideal}}[n(\mathbf{r})] + F_{\text{HS}}[n(\mathbf{r})] + F_{\text{disp}}[n(\mathbf{r})] + F_{\text{assoc}}[n(\mathbf{r})] \tag{5.1}$$

where F_{ideal} is the ideal gas free energy and F_{HS} is the hard-sphere excess free energy, for which we use the White Bear functional [59]. F_{disp} is the free energy contribution due to the square-well dispersion interaction; this term contains one empirical parameter, s_d, which is used to fit the surface tension of water near one atmosphere. Finally, F_{assoc} is the free energy contribution due to association, which is the term that we examine in this chapter.

5.2.1 Dispersion

The dispersion term in the free energy includes the van der Waals attraction and any orientation-independent interactions. Following Hughes *et al.*, we use a dispersion term based on the SAFT-VR approach [86], which has two free parameters (taken from Clark *et* al. [72]): an interaction energy ϵ_d and a length scale $\lambda_d R$.

The SAFT-VR dispersion free energy has the form [86]

$$F_{\text{disp}}[n] = \int \left(a_1(\mathbf{x}) + \beta a_2(\mathbf{x})\right) n(\mathbf{x}) d\mathbf{x} \tag{5.2}$$

where a_1 and a_2 are the first two terms in a high-temperature perturbation expansion and $\beta = 1/k_B T$. The first term, a_1, is the mean-field dispersion interaction. The second term, a_2, describes the effect of fluctuations resulting from compression of the fluid due to the dispersion interaction itself, and is approximated using the local compressibility approximation (LCA), which assumes the energy fluctuation is simply related to the compressibility of a hard-sphere reference fluid [87].

The form of a_1 and a_2 for SAFT-VR is given in reference [86], expressed in terms of the packing fraction. In order to apply this form to an *inhomogeneous* density distribution, we construct an effective local packing fraction for dispersion η_d, given by a Gaussian convolution of the density:

$$\eta_d(\mathbf{x}) = \frac{1}{6\sqrt{\pi}\lambda_d^3 s_d^3} \int n(\mathbf{x}') \exp\left(-\frac{|\mathbf{x} - \mathbf{x}'|^2}{2(2\lambda_d s_d R)^2}\right) d\mathbf{x}'. \tag{5.3}$$

This effective packing fraction is used throughout the dispersion functional, and represents a packing fraction averaged over the effective range of the dispersive interaction. Eq. 5.3 contains an additional empirical parameter s_d introduced by Hughes *et al.*, which modifies the length scale over which the dispersion interaction is correlated.

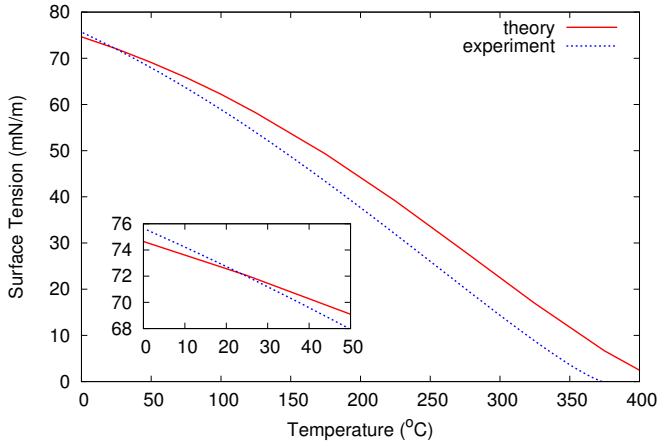

Figure 5.1: Comparison of Surface tension versus temperature for theoretical and experimental data. The experimental data is taken from NIST [5]. The length-scaling parameter s_d is fit so that the theoretical surface tension will match the experimental surface tension near room temperature.

5.2.2 Association

The association free energy for our four-site model has the form:

$$F_{\text{assoc}}[n] = k_B T \int n_{\text{site}}(\mathbf{x}) \left(\ln X(\mathbf{x}) - \frac{X(\mathbf{x})}{2} + \frac{1}{2} \right) d\mathbf{x} \tag{5.4}$$

where $n_{\text{site}}(\mathbf{r})$ is the density of bonding sites at position $\mathbf{r}$:

$$n_{\text{site}}(\mathbf{r}) = \begin{cases} 4n(\mathbf{r}) & \text{this work} \\ 4n_0(\mathbf{r})\zeta(\mathbf{r}) & \text{Hughes } \textit{et al.} \text{ [63]} \end{cases} \tag{5.5}$$

where the factor of four comes from the four hydrogen bond sites, the fundamental measure $n_0(\mathbf{r})$ is the average density contacting point $\mathbf{r}$, and $\zeta(\mathbf{x})$ is a dimensionless

measure of the density inhomogeneity from Yu and Wu [4], defined in Eq 4.27. The functional $X(\mathbf{r})$ is the fraction of association sites *not* hydrogen-bonded, which is determined for our 4-site model by the quadratic equation

$$X(\mathbf{x}) = \frac{\sqrt{1 + 2n'_{\text{site}}(\mathbf{r})\kappa_a g_\sigma^{SW}(\mathbf{x})\left(e^{\beta\epsilon_a} - 1\right)} - 1}{n'_{\text{site}}(\mathbf{r})\kappa_a g_\sigma^{SW}(\mathbf{x})\left(e^{\beta\epsilon_a} - 1\right)}, \tag{5.6}$$

where

$$n'_{\text{site}}(\mathbf{r}) = \begin{cases} \frac{4}{\pi\sigma^2}\int n(\mathbf{r}')\delta(\sigma - |\mathbf{r} - \mathbf{r}'|)d\mathbf{r}' & \text{this work} \\ 4n_0(\mathbf{r})\zeta(\mathbf{r}) & \text{Hughes } \textit{et al.} \end{cases} \tag{5.7}$$

is the density of bonding sites that could bond to the sites $n_{\text{site}}(\mathbf{r})$, and

$$g_\sigma^{SW}(\mathbf{x}) = g_\sigma^{HS}(\mathbf{x}) + \frac{1}{4}\beta\left(\frac{\partial a_1}{\partial \eta_d(\mathbf{x})} - \frac{\lambda_d}{3\eta_d}\frac{\partial a_1}{\partial \lambda_d}\right), \tag{5.8}$$

where g_σ^{HS} is the correlation function evaluated at contact for a hard-sphere fluid, and a_1 and a_2 are the two terms in the dispersion free energy given in Eq. 5.2. The radial distribution function of the square-well fluid g_σ^{SW} is constructed as a perturbative correction to the hard-sphere radial distribution function g_σ^{HS}. The functional of Hughes *et al.* uses the g_σ^{HS} from Yu and Wu [4]. In this work, we use the g_σ^{HS} derived in Chapter 4.

As in Hughes *et al.*, we use Clark's five empirical parameters, and fit the calculated surface tension to experimental surface tension at ambient conditions by tuning the parameter s_d, which adjusts the length-scale of the average density

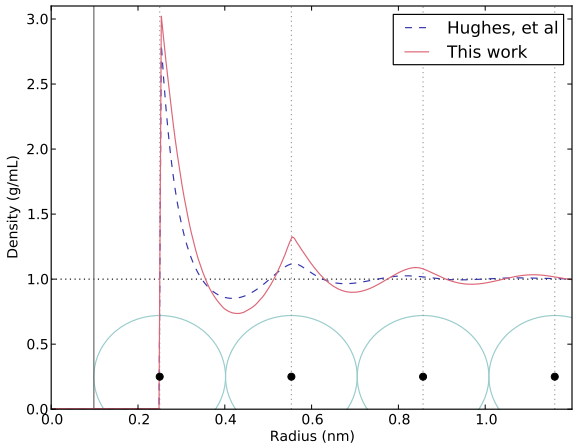

Figure 5.2: Density profiles for a water around a single hard rod of radius 0.1 nm. The solid red profile is from the functional developed in this chapter and the dashed blue profile is the result from Hughes *et al.*. For scale, under the profiles is a cartoon of a string of hard spheres touching in one dimension. The horizontal black dotted line is the bulk density for water and the vertical line on the left at 0.1 nm represents the rod wall.

used for the dispersion interaction. With the improved association term, we find these agree when s_d is 0.454, which is an increase from the value of 0.353 found by Hughes *et al.*. In order to explore further the change made by the improved association term, we compared the new functional with that of Hughes *et al.* for the two hydrophobic cases of the hard rod and the hard spherical solute.

5.3 Results

We will first discuss the case of a single hard rod immersed in water. Figure 5.2 shows the density profile of water near a rod with radius 1 Å. The density computed

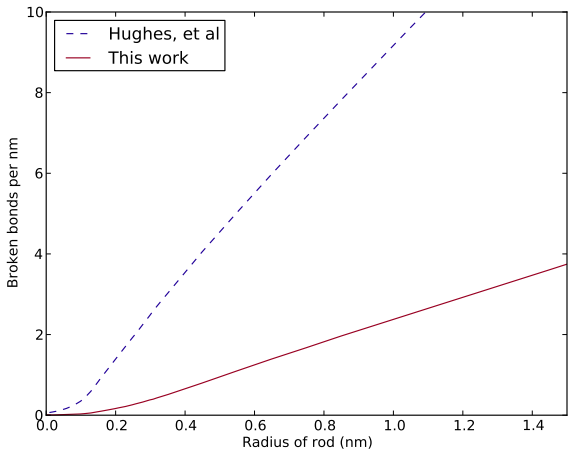

Figure 5.3: Broken hydrogen bonds per nanometer for hard rods immeresed in water. The solid red line uses the functional developed in this chapter while the dashed blue line uses the functional from Hughes *et al.*. For large enough rods, the graph increases linearly for both functionals.

using the functional of this chapter is qualitatively similar to that from Hughes *et al.*, with a comparable density at contact—consistent with having made only a moderate change in the free energy. The first density peak near the surface is higher than that from Hughes *et al.*, and the peak has a kink at the top. This reflects the improved accuracy of the g_σ^{HS} compared with Hughes *et al.*, since beyond the first peak water molecules are unable to touch—or hydrogen bond to—molecules at the surface of the hard rod. This is illustrated under the profiles in Figure 5.2 by a cartoon of adjacent hard spheres that are increasingly distant from the hard rod surface.

In addition to the density, we examine the number of hydrogen bonds which

are broken due to the presence of a hard rod. We define this quantity as

$$N_{\text{broken HB}} = 2 \int (X(\mathbf{r}) - X_{\text{bulk}}) n_{\text{site}}(\mathbf{r}) d\mathbf{r} \tag{5.9}$$

where $X_{\text{bulk}} = 0.13$ is the fraction of unbonded association sites in the bulk. The factor of 2 is chosen to account for the four association sites per molecule, and the fact that each broken hydrogen bond must be represented twice—once for each of the molecules involved. In Fig. 5.3 we show the number of hydrogen bonds broken by a hard rod per nanometer length, as predicted by the functional of Hughes *et al.* (dashed line) and this work (solid line), as a function of the radius of the hard rod. In each case in the limit of large rods, the number of broken bonds is proportional to the surface area. At every radius, the functional of Hughes *et al.* predicts approximately four times as many broken hydrogen bonds as the improved functional.

A common test case for studying hydrophobic solutes in water is the hard-sphere solute. Figure 5.4 shows results for the number of broken hydrogen bonds caused by a hard-sphere solute, as a function of the solute radius. As in Fig. 5.3, the number of broken bonds scales with surface area for large solutes, and the number of broken bonds is about four times smaller than the number from the functional of Hughes *et al.*. For solutes smaller than 3 Å in radius, there is less than a tenth of a hydrogen bond broken. This is consistent with the well-known fact that small solutes (unlike large solutes) do not disrupt the hydrogen-bonding network of water [88].

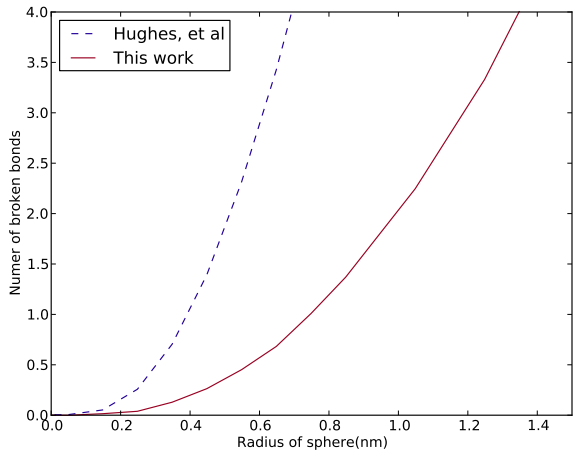

Figure 5.4: Broken hydrogen bonds for hard spheres immeresed in water. The solid red line uses our the functional developd in this chapter while the dashed blue line is from Hughes *et al.*.

Finally, in order to compare with experimental results, we examined the hydration of Krypton. To describe the interaction of water with krypton, we use a Lennard-Jones potential with values $\epsilon = .9518$ kJ/mol and $\sigma = 3.42$ Å calculated using the Lorentz-Berthelot mixing rules and the Lennard-Jones parameters for water from SPC/E calculations [89]. Figure 5.5 shows the krypton-oxygen partial radial distribution function $g_{Kr-O}(r)$, which gives the relative probability density that an oxygen atom resides at a distance r from a krypton atom centered at the origin. We present theoretical curves computed using both this work and the functional of Hughes *et al.*, which we compare with experimental data from extended x-ray absorption fine structure spectroscopy (EXAFS) [6]. The new functional shows improved agreement with experiment in the height and position of the first

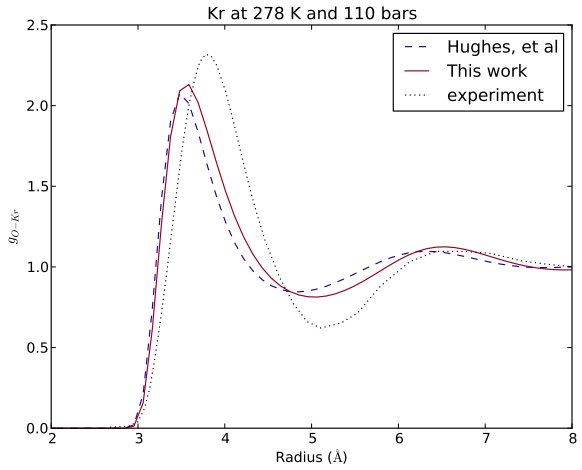

Figure 5.5: The Kr-O partial radial distribution function at low temperature (5° C) and high pressure (110 bar) in the limit of low concentration of krypton in water. The dashed blue line is computed using using the functional from Hughes *et al.*, the solid red line is this work, and the black dotted line is from experiment [6].

maximum as well as the hight and position of the first minimum in $g_{Kr-O}(r)$ when compared with that of Hughes *et al.*

5.4 Conclusion

We have modified the classical DFT for water developed by Hughes *et al.* [63] with the more accurate radial distribution function at contact developed in Chapter 4, which affects the predicted hydrogen bonding between water molecules. We found that while this modification has a relatively mild effect on the free energy and density profiles, it predicts fewer broken hydrogen bonds around hard hydrophobic solutes and at aqueous interfaces. The improved functional does indeed show better

agreement with experiment when used to compute the partial radial distribution function of a krypton atom dissolved in water.

6 Pair Distribution Function

6.1 Introduction

In this chapter we introduce an approximation for the pair distribution function of the inhomogeneous hard sphere fluid. Our approximation makes use of our recently published averaged pair distribution function at contact, detailed in chapter 4, which has been shown to accurately reproduce the averaged pair distribution function at contact for inhomogeneous density distributions. This approach achieves greater computational efficiency than previous approaches by enabling the use of exclusively fixed-kernel convolutions and thus allowing an implementation using fast Fourier transforms. We compare results for our pair distribution approximation with two previously published works and Monte-Carlo simulation, showing favorable results.

Within standard liquid state theory, the perturbation theory treatment of intermolecular interactions relies on the pair distribution function of the reference fluid: $g^{(2)}_{HS}(\mathbf{r}_1, \mathbf{r}_2)$. Unlike the radial distribution function of a homogeneous fluid, there does not currently exist a tractable form for the pair distribution function of an inhomogeneous hard-sphere fluid, suitable for use in constructing a density functional [75, 90].

At its core, thermodynamic perturbation theory (TPT), sometimes referred to as the high-temperature expansion, is an expansion of the free energy in powers of

a small parameter, which is the product of a pairwise attractive interaction with the inverse temperature β:

$$F = F_0 + F_1 + \beta F_2 + \mathcal{O}(\beta^2) \tag{6.1}$$

where the terms F_n are corrections to the free energy of order n in the small interaction. The first and largest term in this expansion is

$$F_1[n(\mathbf{r})] = \tfrac{1}{2} \iint g^{(2)}_{HS}(\mathbf{r}_1, \mathbf{r}_2) n(\mathbf{r}_1) n(\mathbf{r}_2) \Phi(|\mathbf{r}_1 - \mathbf{r}_2|) d\mathbf{r}_1 d\mathbf{r}_2 \tag{6.2}$$

where $g^{(2)}_{HS}(\mathbf{r}_1, \mathbf{r}_2)$ is the pair distribution function of the hard-sphere reference fluid, and $\Phi(r)$ is the pair potential. Formally, this requires the pair distribution function as a functional of the density $n(\mathbf{r})$. In Section 6.2, we introduce existing theoretical approaches for computing $g^{(2)}_{HS}(\mathbf{r}_1, \mathbf{r}_2)$ given the external potential felt by the hard spheres. In Section 6.3, we introduce existing approximations for the hard-sphere pair distribution that are expressed as a functional of the density distribution $n(\mathbf{r})$, which is a form that is more directly useful in the construction of classical density functionals—which are themselves expressed as a functional of the density.

In this chapter, we introduce a new contact value approach (CVA) to approximating the hard-sphere pair distribution function which is suitable for use in the creation of classical density functionals based on thermodynamic perturbation theory. The resulting function is based on a fit to the radial distribution function that is separable in a way that enables efficient evaluation of the integral in Eq. 6.2.

6.2 Pair distribution from the external potential

Given the external potential $V(\mathbf{r})$ felt by a hard-sphere fluid, there are several approaches that have been used to compute the pair distribution function. We review these approaches here. The classic (and earliest) approach for computing the pair distribution function given the external potential is Percus' trick of treating one sphere as an additional contribution to the external potential, and to find the pair distribution function from the resultant equilibrium density [45]. This elegant approach lends itself to computation *using* DFT, and can be used to compute and plot the pair distribution function, but requires a full free-energy minimization *for each position* $\mathbf{r}_1$ in $g^{(2)}(\mathbf{r}_1, \mathbf{r}_2)$, and hence would be prohibitively expensive as a tool in constructing a free energy functional.

The canonical inhomogeneous configuration for the hard-sphere fluid is the system consisting of a hard sphere at a hard wall. In 1986, Plischke and Henderson solved the pair distribution function of this system using integral equation theory under the Percus-Yevick approximation [91]. Lado recently introduced a new and more efficient algorithm for implementing integral equation theory for inhomogeneous fluids, which computes $g^{(2)}(\mathbf{r}_1, \mathbf{r}_2)$ [92]. While this approach is two orders of magnitude more efficient than previous implementations, it remains a computationally expensive approach, and unsuitable for repeated evaluation within a free-energy minimization as required by DFT.

Another inhomogeneous configuration that is of interest is the test-particle configuration, in which one hard sphere is fixed. Where the hard-wall is a sur-

face with no curvature, the test-particle configuration has a surface with curvature at the molecular length scale. In this case, the density gives the radial distribution function—this is just Percus' trick—and the pair distribution function of this inhomogeneous test-particle system gives the triplet distribution function of the homogeneous fluid. The triplet distribution function of the homogeneous fluid has been computed by González *et al.* using the test-particle approach with *two* spheres fixed [93].

6.3 Pair distribution from the density

The alternative to specifying the external potential is to specify the density distribution $n(\mathbf{r})$. One may move between these representations by either computing the external potential corresponding to a given density of hard spheres by taking a functional derivative of the hard-sphere free energy functional, or by minimizing the free energy given an external potential. However, in general it is simplest to use an approach that makes use of the natural variables, which in the case of classical density functional theory is the density.

The most direct and rigorous approach to find the pair distribution function given the density is to take a second functional derivative of the hard-sphere free energy to find the direct correlation function. One can then solve the Ornstein-Zernike equation numerically to find the pair distribution function. This approach was used by Götzelmann *et al.* to solve for the pair distribution function near a hard wall using an early hard-sphere free energy functional [94]. While this ap-

proach is rigorous, solving the inhomogeneous Ornstein-Zernike equation remains computationally challenging, although more efficient approximate algorithms have been developed [95]. This approach, while appealing, remains unsuitable for use in the construction of a classical density functional due to its significant computational cost.

In addition to the above exact approach, there are a number of analytic approximations for the inhomogeneous pair distribution function, which extend the radial distribution function to inhomogeneous scenarios. These approximations differ both in what density to use when evaluating the radial distribution function $g(r; n)$, and in how to combine the radial distribution function evaluated at these densities [96].

Early approximations to the pair distribution function used the density at one or two positions to determine the pair distribution function. There are three common approaches:

$$g^{(2)}(\mathbf{r}_1, \mathbf{r}_2) \approx g\left(r_{12}; n\left(\frac{\mathbf{r}_1 + \mathbf{r}_2}{2}\right)\right) \qquad \text{midpoint} \tag{6.3}$$

$$g^{(2)}(\mathbf{r}_1, \mathbf{r}_2) \approx g\left(r_{12}; \frac{n(\mathbf{r}_1) + n(\mathbf{r}_2)}{2}\right) \qquad \text{mean density} \tag{6.4}$$

$$g^{(2)}(\mathbf{r}_1, \mathbf{r}_2) \approx \frac{g(r_{12}; n(\mathbf{r}_1)) + g(r_{12}; n(\mathbf{r}_2))}{2} \qquad \text{mean function} \tag{6.5}$$

These approaches have been successfully and widely used in treating the surface tension of simple fluids [97–105]. The mean density approximation has also been quoted (as a goal) by recent papers that proceed to make further approximations [3,

75]. However, these approximations fail dramatically when applied to strongly inhomogeneous systems such as a dense fluid at a solid surface. Such systems exhibit a strongly oscillatory density distribution, with density peaks that can have local packing fractions greater than unity, which cannot occur in the bulk reference system that defines $g(r; n)$. The above papers restrict themselves to the liquid-vapor interface, which does not exhibit this pathology.

Non-pathological approaches use an average of the density over some volume. Fischer and Methfessel introduce the approximation [9, 106]:

$$g^{(2)}(\mathbf{r}_1, \mathbf{r}_2) \approx g\left(r_{12}; n_3\left(\tfrac{1}{2}(\mathbf{r}_1 + \mathbf{r}_2)\right)\right) \tag{6.6}$$

where n_3 is an integral of the density over a spherical volume that is now used as one of the fundamental measures in Fundamental Measure Theory [52]:

$$n_3(\mathbf{r}) = \int n(\mathbf{r}')\Theta(\tfrac{1}{2}\sigma - |\mathbf{r} - \mathbf{r}'|)d\mathbf{r}' \tag{6.7}$$

Equation 6.6 is computationally awkward, because it treats as special the midpoint $\frac{1}{2}(\mathbf{r}_1+\mathbf{r}_2)$. Moreover, the approach of Fischer and Methfessel is intended to approximate the pair distribution function only at contact, when the distance between $\mathbf{r}_1$ and $\mathbf{r}_2$ is the hard-sphere diameter. Tang *et al.* employed an approximation for the pair distribution function that is similar to that of Fischer and Methfessel, but with a self-consistent weighted density computed with a weighting function that is itself dependent on the weighted density [107]. This weighted density was computed using the hard-sphere weighted density of Tarazona, which was developed

using the direct correlation function of the homogeneous hard-sphere fluid [108].

Sokolowski and Fischer addressed the shortcomings of the theory of Fischer and Methfessel by modifying this approach to use density averages centered on the two points $\mathbf{r}_1$ and $\mathbf{r}_2$:

$$g^{(2)}(\mathbf{r}_1, \mathbf{r}_2) \approx g\left(r_{12}; \tfrac{1}{2}(\bar{n}(\mathbf{r}_1) + \bar{n}(\mathbf{r}_2))\right) \tag{6.8}$$

where their averaged density $\bar{n}(\mathbf{r})$ given by

$$\bar{n}(\mathbf{r}) \equiv \frac{3}{4\pi(0.8\sigma)^3} \int n(\mathbf{r}')\Theta(0.8\sigma - |\mathbf{r} - \mathbf{r}'|)d\mathbf{r}' \tag{6.9}$$

is the density averaged over a sphere with diameter 0.8σ [8]. The value 0.8 in this formula was arrived at by fitting to Monte Carlo simulation. Although Eq. 6.8 has the advantage of only involving density averages at the points at which the pair distribution function is desired, it remains sufficiently computationally cumbersome that it has only been used in two papers studying the one-dimensional liquid vapor interface [109,110]. Because it cannot be written as a single-site convolution, this approach is particularly computationally demanding when applied to systems featuring inhomogeneity in more than one dimension.

In Chapter 4, we introduce a functional that gives a good approximation for the pair distribution function averaged over positions $\mathbf{r}_2$ that are in contact with

$\mathbf{r}_1$, defined as:

$$g_\sigma(\mathbf{r}_1) \equiv \frac{\int g^{(2)}(\mathbf{r}_1, \mathbf{r}_2)\delta(\sigma - |\mathbf{r}_1 - \mathbf{r}_2|)n(\mathbf{r}_2)d\mathbf{r}_2}{\tilde{n}(\mathbf{r}_1)} \tag{6.10}$$

where the weighted density $\tilde{n}(\mathbf{r}_1)$ is defined by:

$$\tilde{n}(\mathbf{r}) \equiv \int n(\mathbf{r}')\delta(\sigma - |\mathbf{r} - \mathbf{r}'|)d\mathbf{r}'. \tag{6.11}$$

In Chapter 4 we use the contact-value theorem to derive the exact formula:

$$g_\sigma(\mathbf{r}) = \frac{1}{2}\frac{1}{k_B T n(\mathbf{r})\tilde{n}(\mathbf{r})}\frac{\delta F_{HS}}{\delta\sigma(\mathbf{r})} \tag{6.12}$$

where $\sigma(\mathbf{r})$ is the diameter of hard spheres located at position $\mathbf{r}$, and F_{HS} is the Helmholtz free energy of the hard-sphere fluid. The functional derivative of the free energy with respect to the hard-sphere diameter in Eq. 6.12 requires that we be able to evaluate the change in free energy resulting from a change in the diameter of specifically the hard spheres located at position $\mathbf{r}$. This somewhat unusual construction is mathematically straightforward within Fundamental Measure Theory (FMT) [52]. We employ the White Bear variation of the FMT free energy functional [59], which provides an excellent approximation for this averaged value of the pair distribution function at contact for a variety of interfaces, and over a wide range of densities.

6.4 Contact value approach

In the approaches for the pair distribution function mentioned above, the radial distribution function used in the approximation was dependent upon the density averaged over some volume. We seek to achieve greater accuracy by making use of a function dependent upon our averaged $g_\sigma(\mathbf{r})$ discussed above, which holds more information about an inhomogeneous system than does a simple convolution of the density. We construct the CVA with the average of two radial distribution functions, evaluated at the distance between the two points, that are themselves functions of the averaged pair distribution function at contact $g_\sigma(\mathbf{r})$ evaluated at the two points:

$$g^{(2)}(\mathbf{r}_1, \mathbf{r}_2) = \frac{g(r_{12}; g_\sigma(\mathbf{r}_1)) + g(r_{12}; g_\sigma(\mathbf{r}_2))}{2}. \tag{6.13}$$

This CVA for $g^{(2)}(\mathbf{r}_1, \mathbf{r}_2)$ is constructed to reproduce the exact value for the integral:

$$F_1^{\text{contact}} = \tfrac{1}{2} \iint g_{HS}^{(2)}(\mathbf{r}_1, \mathbf{r}_2) n(\mathbf{r}_1) n(\mathbf{r}_2) \delta(|\mathbf{r}_1 - \mathbf{r}_2| - \sigma) d\mathbf{r}_1 d\mathbf{r}_2 \tag{6.14}$$

which is the mean-field correction to the free energy (see Eq. 6.2) for a purely contact interaction.

The CVA requires the radial distribution function expressed as a function of r and g_σ. We construct a functional form for $g(r, g_\sigma)$ that allows for improved computational efficiency. We introduce the general form that allows for this efficiency in Section 6.5, and we detail our specific approximation for $g(r, g_\sigma)$ that uses this

general form in Section 6.6.

6.5 Making the CVA efficient

The existing approaches to approximating the pair distribution function outlined in Section 6.3 have not been widely used in the construction of density functionals based on thermodynamic perturbation theory, largely due to their computational complexity. While our CVA provides only an incremental improvement in accuracy, its construction enables significant gains in computational efficiency, allowing for practical application in density functionals. We achieve this gain by developing a *separable* fit to the radial distribution function of the hard-sphere fluid (see Section 6.6 for details). This separable fit is of the form

$$g(r; g_\sigma) = \sum_i a_i(r) b_i(g_\sigma) \tag{6.15}$$

where the notable aspect is that the radial distribution function is written as a sum of terms that are each a simple product of a function of radius with a function of g_σ. This enables us to write integrals—such as Eq. 6.2—that are linear in the pair distribution function as a summation of fixed-kernel convolutions, which may be efficiently computed using Fast Fourier Transforms (FFTs).

Computation of the free energy correction from Eq. 6.2 for a periodic system by direct integration requires a nested integration over the volume of the system V_{cell}, and the volume over which the interaction is nonzero V_Φ. Thus the cost

of computation scales as $\mathcal{O}\left(\frac{V_{cell}V_\Phi}{\Delta V^2}\right)$ where ΔV is the volume resolution of the computational grid. Direct integration is the most efficient algorithm when using the existing functionals for $g^{(2)}(\mathbf{r}_1, \mathbf{r}_2)$ described in Section 6.3. The one exception is the "mean-function" approximation (Eq. 6.5), which could in principle be made more efficient using the same technique we describe here. Because the CVA allows the integral in Eq. 6.2 to be written as a sum of fixed-kernel convolutions, it can be computed without a nested integral, at the cost of performing a few FFTs. This approach scales as $\mathcal{O}\left(\frac{V_{cell}}{\Delta V}\log\frac{V_{cell}}{\Delta V}\right)$, as do most widely used DFT functionals such as FMT [52, 59]. With this scaling, when examining systems with long interaction distances or high resolution—which is often necessary when working with hard-sphere functionals—the CVA has the potential to be far more efficient than existing methods.

To see how we obtain this improved scaling, we examine the lowest-order correction in TPT, given by Eq. 6.2. The two terms that are averaged in Eq. 6.13 give equal contributions to the integral

$$F_1^{CVA} = \tfrac{1}{2}\iint g(r_{12}; g_\sigma(\mathbf{r}_2))n(\mathbf{r}_1)n(\mathbf{r}_2)\Phi(|\mathbf{r}_1 - \mathbf{r}_2|)d\mathbf{r}_1 d\mathbf{r}_2. \tag{6.16}$$

When we introduce the separable form for $g(r_{12}; g_\sigma)$ we can further simplify this integral as

$$F_1^{CVA} = \sum_i \tfrac{1}{2}\int n(\mathbf{r}_1)\int a_i(r_{12})\Phi(r_{12})b_i(g_\sigma(\mathbf{r}_2))n(\mathbf{r}_2)d\mathbf{r}_2 d\mathbf{r}_1 \tag{6.17}$$

where the functional is written as a summation of integrals of simple convolutions

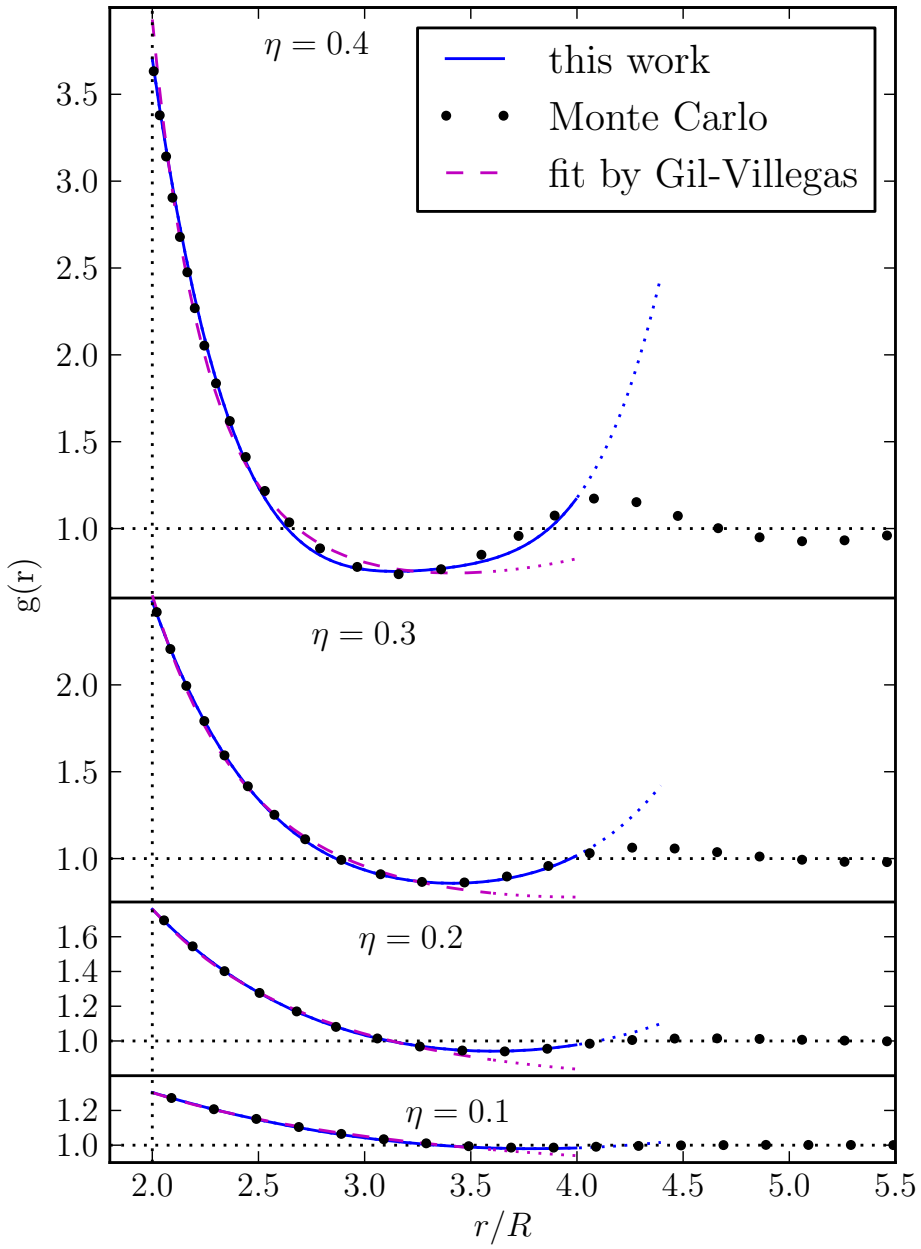

Figure 6.1: Plot of the hard-sphere radial distribution function of the homogeneous fluid at several values for packing fraction η. The blue lines show our separable fit, the black dots show the true radial distribution function $g(r)$ as found from Monte Carlo simulation, and the dashed lines are results of the Gil-Villegas fit [7]. The dotted extension of each fitted curve indicates the value of the function outside of the fitted region.

in three dimensions. Thus, each of these integrals may be computed in $\mathcal{O}(N \log N)$ time, where N is the number of grid points in the computational cell. This is the same scaling as is required to compute the fundamental measures such as n_3 which are used in FMT.

6.6 A separable fit for the radial distribution function

Having settled on the basic structure of our function, we further refine it by performing a separable fit to the radial distribution function from Monte Carlo simulation. We focus our fit on the range of distances $r_{12} \leq 4R$. This range is relevant to the widely used [46–48] Statistical Associating Fluid Theory of Variable Range (SAFT-VR) free energy with square-well dispersive attraction developed by Gil-Villegas *et al.* [7]. Although we consider this range of radii particularly interesting, this is not a fundamental limit of the approach, as one could readily extend the fit to larger radii by including additional fitting parameters. For comparison, in Fig. 6.1 we plot our fit, Monte-Carlo data, and the radial distribution function of Gil-Villegas *et al.*, which we have extracted from their approximation for the first term in the dispersion free energy given by Eq. 6.2.

For ease of implementation and future extension to larger radii, we fit the radial distribution function using a fourth-order polynomial. We constrain our functional form such that $g(r; g_\sigma)$ reduces to g_σ at contact and approaches $g(r) = 1$ in the

$$\kappa = \begin{pmatrix} -1.754 & 0.027 & 0.838 & -0.178 \\ -2.243 & 4.403 & -2.48 & 0.363 \\ 0.207 & 0.712 & -1.952 & 1.046 \\ -0.002 & -0.164 & 0.324 & -0.162 \end{pmatrix}$$

Table 6.1: The fitted κ_{ij} matrix.

low-density limit. Incorporating these constraints we have the functional form

$$g(r; g_\sigma) = g_\sigma + \sum_{i=1}^{4} \sum_{j=1}^{4} \kappa_{ij} (g_\sigma - 1)^i \left(\tfrac{r}{\sigma} - 1\right)^j , \tag{6.18}$$

where the matrix κ_{ij} is determined from a least-squares fit to Monte Carlo data for the radial distribution function, over the range $2R \leq r \leq 4R$, and for packing fractions $\eta \leq 0.45$. The resulting parameters are displayed in Table 6.1. The maximum error in $g(r)$ within this range is 0.2, which occurs at $\eta = 0.45$ and $r = 3.7R$. Fig. 6.1 displays our approximation at just under half of the densities that were included in the fit.

6.7 Results

6.7.1 Pair distribution function

We begin by examining the pair distribution function near a hard wall, with a focus on the case where one of the two spheres is in contact with the hard wall. Figures 6.2a and 6.2c compare the results of the CVA with Monte Carlo simulations

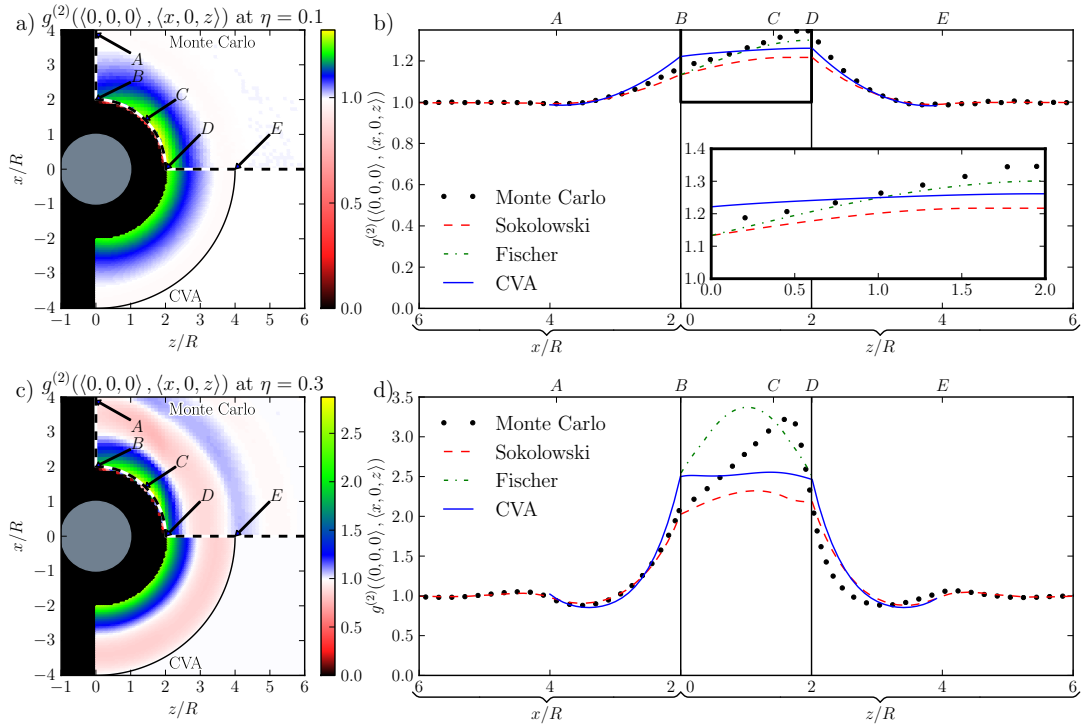

Figure 6.2: The pair distribution function near a hard wall, with packing fractions of 0.1 and 0.3 and $\mathbf{r}_1$ in contact with the hard wall. On the left are 2D plots of $g^{(2)}(\mathbf{r}_1, \mathbf{r}_2)$ as $\mathbf{r}_2$ varies. The top halves of these figures show the results of Monte Carlo simulations, while the bottom halves show the CVA, truncated beyond the range of the fit. On the right are plots of $g^{(2)}(\mathbf{r}_1, \mathbf{r}_2)$ on the paths illustrated in the figures to the left. These plots compare the CVA (blue solid line), Monte Carlo results (black circles), the results of Sokolowski and Fischer (red dashed line) [8], and those of Fischer and Methfessel (green dot-dashed line) [9]. The latter is only plotted at contact, where it is defined.

at packing fractions of 0.1 and 0.3 respectively. We see reasonable agreement at the lower density, with a flatter angular dependence when the two spheres are in contact. At the higher density, we see significant structure developing in the simulation results that is not reflected in our approximation.

Figures 6.2b and 6.2d show the pair distribution function as plotted along paths illustrated in Figures 6.2a and 6.2c. These plots compare the CVA with Monte Carlo results, as well as the approximations of Sokolowski and Fischer [8] and of Fischer and Methfessel [9] at the same packing fractions of 0.1 and 0.3. The approach of Fischer and Methfessel is only defined when the two spheres are in contact, and is therefore only plotted on that segment of the path. As an input to the previous approximations we use the hard sphere radial distribution function found with Monte Carlo simulation, interpolated as necessary. We find that both previous approximations to the pair distribution function predict stronger angular dependence of the pair distribution function at contact than this work. The previous approximations each have a systematic error at contact—either too high or too low. In contrast, our errors at contact have a tendency to cancel when used in a perturbation expansion. At higher densities, the approximation of Fischer and Methfessel requires evaluating the radial distribution function at densities significantly higher than the freezing density, which poses numerical difficulties when using the radial distribution function from simulation. When the two points $\mathbf{r}_1$ and $\mathbf{r}_2$ are both more than a radius away from contact, we find that any of these approaches gives a reasonable prediction.

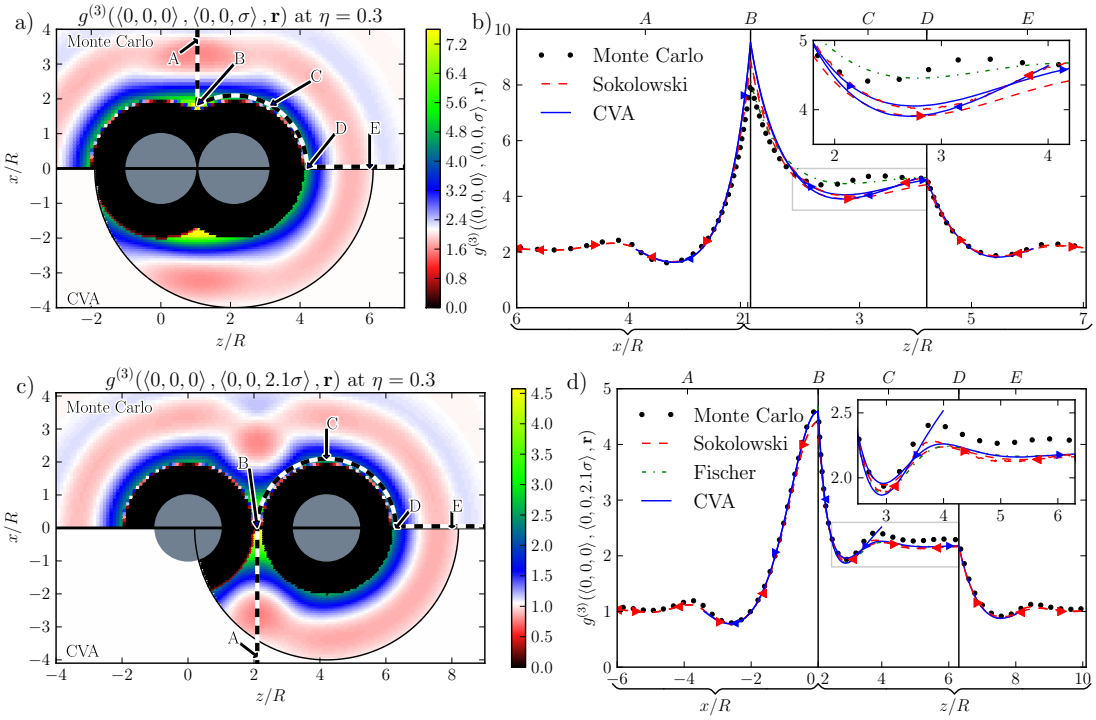

Figure 6.3: The triplet distribution function $g^{(3)}(\mathbf{r}_1, \mathbf{r}_2, \mathbf{r}_3)$ at packing fraction 0.3, plotted when $\mathbf{r}_1$ and $\mathbf{r}_2$ are in contact (a,b) and when $\mathbf{r}_1$ and $\mathbf{r}_2$ are separated by a distance 2.1σ (c,d). On the left are 2D plots of $g^{(3)}(\mathbf{r}_1, \mathbf{r}_2, \mathbf{r}_3)$ as $\mathbf{r}_3$ varies. The top halves of these figures show the results of Monte Carlo simulations, while the bottom halves show the CVA, truncated beyond the range of the fit. On the right are plots of $g^{(3)}(\mathbf{r}_1, \mathbf{r}_2, \mathbf{r}_3)$ on the paths illustrated in the figures to the left. We also plot these curves along a left-right mirror image of this path. The data for the right-hand paths (as shown in the 2D images) are marked with right-pointing triangles, while the left-hand paths are marked with left-pointing triangles.

6.7.2 Triplet distribution function

Just as the radial distribution function of a homogeneous fluid may be computed from the density of an inhomogeneous one using Percus' test-particle trick, the triplet distribution function of a homogeneous system can be computed using an approximation of the pair distribution for an inhomogeneous fluid, such as we have developed. The triplet distribution function of a homogeneous fluid with density n is given by:

$$g^{(3)}(\mathbf{r}_1, \mathbf{r}_2, \mathbf{r}_3) = \frac{n_{\mathrm{TP}(\mathbf{r}_1)}(\mathbf{r}_2) n_{\mathrm{TP}(\mathbf{r}_1)}(\mathbf{r}_3)}{n^2} g^{(2)}_{\mathrm{TP}(\mathbf{r}_1)}(\mathbf{r}_2, \mathbf{r}_3) \tag{6.19}$$

where the $\mathrm{TP}(\mathbf{r}_1)$ subscript indicates quantities computed for the inhomogeneous density configuration in which one sphere (the "test particle") is fixed at position $\mathbf{r}_1$. This method treats one of the three positions—the location of the test particle—differently from the other two, which means that a poor approximation to the pair distribution function may break the symmetry between $\mathbf{r}_1$ and $\mathbf{r}_2$ which is present in the true triplet distribution function.

Figures 6.3a and 6.3c compare the triplet distribution function at a packing fraction of 0.3 computed using the CVA with results from Monte Carlo simulations. In Figure 6.3a the spheres at $\mathbf{r}_1$ and $\mathbf{r}_2$ are in contact; in Figure 6.3c they are spaced so that a third sphere can just fit between them; and in both figures $\mathbf{r}_3$ is varied. The test-particle position for the CVA in each case is $\mathbf{r}_1$, which is on the left-hand side of the figure. As before, we see reasonable agreement with simulation. Also, the Monte Carlo results have the expected left-right symmetry, while the CVA

has a small asymmetry introduced with the test particle due to errors in the pair distribution function.

Figures 6.3b and 6.3d show the triplet distribution function as plotted along the paths illustrated in Figures 6.3a and 6.3c. We also plot the results along a left-right mirror image path, corresponding to swapping $\mathbf{r}_1$ and $\mathbf{r}_2$. The two mirror-image paths are distinguished by arrows (triangles) along the curves, with right-facing arrows indicating the paths shown in Figures 6.3a and 6.3c, and left-facing arrows indicating the mirror image path. As the work of Fischer and Methfessel is only defined when $\mathbf{r}_2$ and $\mathbf{r}_3$ are in contact, we only plot it along the central portion of the path, which is in contact with $\mathbf{r}_2$, and arrows are omitted. All methods tested perform similarly over their range of validity.

6.8 Accuracy in thermodynamic perturbation theory

A particularly relevant quantitative test of a pair distribution function is how well it predicts the interaction energy due to a pair potential. To this end, we have computed the error in the first term in a high-temperature perturbation expansion F_1 for two typical pair potentials. In order to focus on effects at the interface, we have defined a position-dependent pair interaction energy as

$$\frac{dF_1}{dz} = \tfrac{1}{2} \int g^{(2)}_{HS}(\mathbf{r}, \mathbf{r}') n(\mathbf{r}) n(\mathbf{r}') \Phi(|\mathbf{r} - \mathbf{r}'|) d\mathbf{r}' \, dxdy \tag{6.20}$$

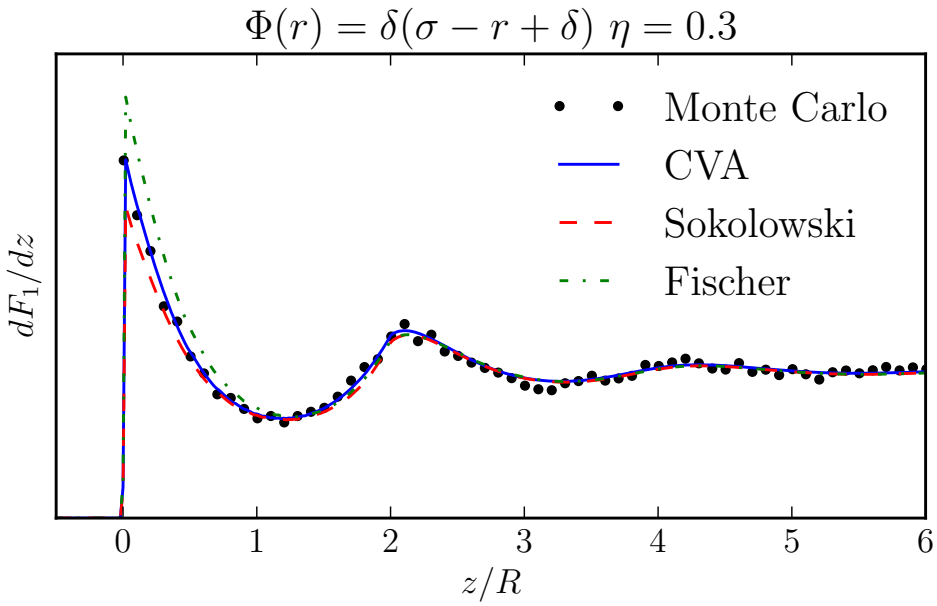

(a) Sticky hard-sphere fluid

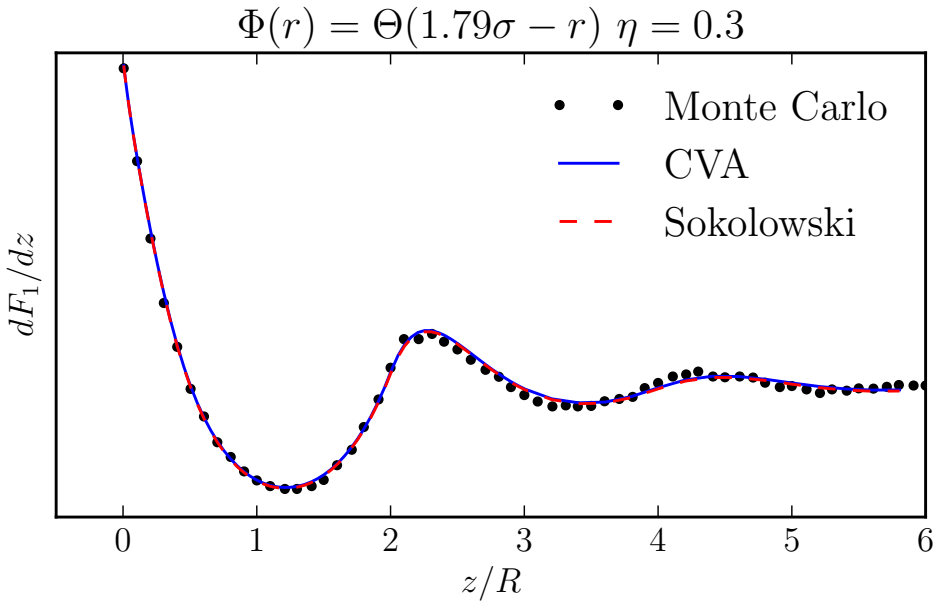

(b) Hard-core square well fluid

Figure 6.4: Plot of $\frac{dF_1}{dz}$ near a hard wall, with arbitrary vertical scale. (a) shows a sticky hard-sphere fluid defined by a pair potential $\delta(\sigma - r + \delta)$ where σ is the hard-sphere diameter, and δ is an infinitesimal distance; and (b) shows a square well fluid defined by a pair potential $\Theta(1.79\sigma - r)$.

which gives the contribution to the mean-field free energy due to molecules located in a plane of fixed z.

We plot this quantity for two representative pair potentials near a hard wall in Fig. 6.4. We have chosen to illustrate a delta-function interaction at contact (i.e. "sticky hard spheres"), and a hard-core square-well fluid, with the length-scale of interaction taken from the optimal SAFT model for water found by Clark *et al.* [72]. These pair potentials represent both a very short-range interaction and a medium-range interaction.

Figure 6.4a shows the results for the sticky hard-sphere fluid. The CVA is constructed to produce this result exactly, provided the averaged pair distribution function at contact from Schulte [85] is exact. As expected, we see excellent agreement with the Monte Carlo simulation results, while the approximations of Fischer and Sokolowski each show deviations near the interface. Figure 6.4b shows the same curve from Eq. 6.20 for the square-well fluid. In this case both the CVA and Sokolowski's approximation give excellent agreement with simulation.

6.9 Conclusion

We have introduced and tested the contact value approach for the pair distribution function $g^{(2)}(\mathbf{r}_1, \mathbf{r}_2)$ of the inhomogeneous hard-sphere fluid. The pair distribution function plays a key role in thermodynamic perturbation theory, which is widely used in the construction of classical density functionals. The CVA—unlike existing approximations—is suitable for use in classical density functionals based on per-

turbation theory, as it may be efficiently computed using exclusively fixed-kernel convolutions. We have tested this function at a hard wall and near a single fixed hard sphere, and find that it gives excellent agreement with simulation. Tests of the pair distribution function in integrals that arise in thermodynamic perturbation theory suggest that the CVA is accurate for attractions up to the distance to which the radial distribution function is fit, and is a significant improvement over existing approximations near contact. But most importantly, the computational cost of using the CVA in a classical density functional scales much more favorably than existing methods in high resolution computations.

7 Conclusion

This dissertation has discussed my investigation into the dynamics of the Min-protein system within E. Coli. We tested a widely-used simulation model [1] in its deterministic and stochastic forms within flattened cells shapes and compared them against recent experimental findings [2]. We found that the deterministic model predicts strong bipolar oscillations, in contradiction with the experimentally observed behavior, while the stochastic model, which is based on the same reaction-diffusion equations, does predict spatially irregular oscillations as observed in experiment. We find as well that it is the flattening and accompanying lateral expansion rather than the asymmetry of the cell shapes that causes the irregular oscillation behavior.

The dissertation then discussed my research in improving free energy functionals that are used within Classical Density Functional Theory in order to model water. In Chapter 4 we defined two averaged values for the distribution function at contact g_σ, and derived formulas for each of them using the White Bear version of the fundamental measure theory functional and the Contact Value Theorem. We tested these formulas, as well as two existing formulas, against Monte Carlo simulations and found excellent agreement between the Monte Carlo data and one of our averaged distribution functions.

In Chapter 5 we examined of the effect of incorporating this function into

our recently published statistical associating fluid theory-based classical density functional theory for water. We studied two hard-sphere solutes and a Lennard-Jones approximation of a krypton-atom solute, and found improvement in the theory.

Finally, in Chapter 6 we derived an approximation for the pair distribution function of the inhomogeneous hard sphere fluid, that uses our g_σ. This approach achieves greater computational efficiency than previous approaches by enabling the use of exclusively fixed-kernel convolutions, which allows for an implementation using fast Fourier transforms. We compared results for our pair distribution approximation with two previously published works and Monte Carlo simulation, and showed favorable results.

Bibliography

[1] Kerwyn Casey Huang, Yigal Meir, and Ned S Wingreen. Dynamic structures in escherichia coli: spontaneous formation of mine rings and mind polar zones. *Proceedings of the National Academy of Sciences*, 100(22):12724–12728, 2003.

[2] Jaan Männik, Fabai Wu, Felix JH Hol, Paola Bisicchia, David J Sherratt, Juan E Keymer, and Cees Dekker. Robustness and accuracy of cell division in escherichia coli in diverse cell shapes. *Proceedings of the National Academy of Sciences*, 109(18):6957–6962, 2012.

[3] J. Gross. A density functional theory for vapor-liquid interfaces using the pcp-saft equation of state. *The Journal of chemical physics*, 131:204705, 2009.

[4] Y. X. Yu and J. Wu. A fundamental-measure theory for inhomogeneous associating fluids. *The Journal of Chemical Physics*, 116:7094, 2002.

[5] E. W. Lemmon, M. O. McLinden, and D. G. Friend. *NIST Chemistry WebBook, NIST Standard Reference Database Number 69*, chapter Thermophysical Properties of Fluid Systems. National Institute of Standards and Technology, Gaithersburg MD, 20899, 2010. http://webbook.nist.gov, (retrieved December 15, 2010).

[6] Daniel T Bowron, Adriano Filipponi, Mark A Roberts, and John L Finney. Hydrophobic hydration and the formation of a clathrate hydrate. *Physical review letters*, 81(19):4164, 1998.

[7] Alejandro Gil-Villegas, Amparo Galindo, Paul J Whitehead, Stuart J Mills, George Jackson, and Andrew N Burgess. Statistical associating fluid theory for chain molecules with attractive potentials of variable range. *The Journal of chemical physics*, 106:4168, 1997.

[8] S Sokolowski and J Fischer. The role of attractive intermolecular forces in the density functional theory of inhomogeneous fluids. *The Journal of chemical physics*, 96(7):5441–5447, 1992.

[9] Johann Fischer and Michael Methfessel. Born-green-yvon approach to the local densities of a fluid at interfaces. *Physical Review A*, 22(6):2836, 1980.

[10] David W Adams and Jeff Errington. Bacterial cell division: assembly, maintenance and disassembly of the z ring. *Nature Reviews Microbiology*, 7(9):642–653, 2009.

[11] Joe Lutkenhaus. Assembly dynamics of the bacterial mincde system and spatial regulation of the z ring. *Annu. Rev. Biochem.*, 76:539–562, 2007.

[12] Bang Shen and Joe Lutkenhaus. Examination of the interaction between ftsz and mincn in e. coli suggests how minc disrupts z rings. *Molecular microbiology*, 75(5):1285–1298, 2010.

[13] Lucy Shapiro, Harley H McAdams, and Richard Losick. Why and how bacteria localize proteins. *Science*, 326(5957):1225–1228, 2009.

[14] Xuan-Chuan Yu and William Margolin. Ftsz ring clusters in min and partition mutants: role of both the min system and the nucleoid in regulating ftsz ring localization. *Molecular microbiology*, 32(2):315–326, 1999.

[15] Giovanni Meacci and Karsten Kruse. Min-oscillations in escherichia coli induced by interactions of membrane-bound proteins. *Physical biology*, 2(2):89, 2005.

[16] Rex A Kerr, Herbert Levine, Terrence J Sejnowski, and Wouter-Jan Rappel. Division accuracy in a stochastic model of min oscillations in escherichia coli. *Proceedings of the National Academy of Sciences of the United States of America*, 103(2):347–352, 2006.

[17] Jaan Männik, Rosalie Driessen, Peter Galajda, Juan E Keymer, and Cees Dekker. Bacterial growth and motility in sub-micron constrictions. *Proceedings of the National Academy of Sciences*, 106(35):14861–14866, 2009.

[18] Brian D Corbin, Xuan-Chuan Yu, and William Margolin. Exploring intracellular space: function of the min system in round-shaped escherichia coli. *The EMBO journal*, 21(8):1998–2008, 2002.

[19] David Fange and Johan Elf. Noise-induced min phenotypes in e. coli. *PLoS computational biology*, 2(6):e80, 2006.

[20] Archana Varma, Kerwyn Casey Huang, and Kevin D Young. The min system as a general cell geometry detection mechanism: Branch lengths in y-shaped escherichia coli cells affect min oscillation patterns and division dynamics. *Journal of bacteriology*, 190(6):2106–2117, 2008.

[21] J Männik, F Sekhavati, JE Keymer, and C Dekker. Bacteria in submicron channels and microvalves. *Proc of MicroTAS 2010, Groningen, The Netherlands*, pages 1346–1348, 2010.

[22] Yoshiki Kuramoto. Diffusion-induced chaos in reaction systems. *Progress of Theoretical Physics Supplement*, 64:346–367, 1978.

[23] Hans Meinhardt and Piet AJ de Boer. Pattern formation in escherichia coli: a model for the pole-to-pole oscillations of min proteins and the localization of the division site. *Proceedings of the National Academy of Sciences*, 98(25):14202–14207, 2001.

[24] Zonglin Hu, Edward P Gogol, and Joe Lutkenhaus. Dynamic assembly of mind on phospholipid vesicles regulated by atp and mine. *Proceedings of the National Academy of Sciences*, 99(10):6761–6766, 2002.

[25] Yu-Ling Shih, Xiaoli Fu, Glenn F King, Trung Le, and Lawrence Rothfield. Division site placement in e. coli: mutations that prevent formation of the mine ring lead to loss of the normal midcell arrest of growth of polar mind membrane domains. *The EMBO journal*, 21(13):3347–3357, 2002.

[26] Mike Bonny, Elisabeth Fischer-Friedrich, Martin Loose, Petra Schwille, and Karsten Kruse. Membrane binding of mine allows for a comprehensive description of min-protein pattern formation. *PLoS computational biology*, 9(12):e1003347, 2013.

[27] Jacob Halatek and Erwin Frey. Highly canalized mind transfer and mine sequestration explain the origin of robust mincde-protein dynamics. *Cell Reports*, 1(6):741–752, 2012.

[28] Giovanni Meacci, Jonas Ries, Elisabeth Fischer-Friedrich, Nicoletta Kahya, Petra Schwille, and Karsten Kruse. Mobility of min-proteins in escherichia coli measured by fluorescence correlation spectroscopy. *Physical biology*, 3(4):255, 2006.

[29] Martin Loose, Elisabeth Fischer-Friedrich, Christoph Herold, Karsten Kruse, and Petra Schwille. Min protein patterns emerge from rapid rebinding and membrane interaction of mine. *Nature structural & molecular biology*, 18(5):577–583, 2011.

[30] Kerwyn Casey Huang and Ned S Wingreen. Min-protein oscillations in round bacteria. *Physical biology*, 1(4):229, 2004.

[31] Karsten Kruse, Martin Howard, and William Margolin. An experimentalist's guide to computational modelling of the min system. *Molecular microbiology*, 63(5):1279–1284, 2007.

[32] Michael J Lawson, Brian Drawert, Mustafa Khammash, Linda Petzold, and Tau-Mu Yi. Spatial stochastic dynamics enable robust cell polarization. *PLoS computational biology*, 9(7):e1003139, 2013.

[33] Matthew L Robb and Vahid Shahrezaei. Stochastic cellular fate decision making by multiple infecting lambda phage. *PloS one*, 9(8):e103636, 2014.

[34] Cihan Oguz, Alida Palmisano, Teeraphan Laomettachit, Layne T Watson, William T Baumann, and John J Tyson. A stochastic model correctly predicts changes in budding yeast cell cycle dynamics upon periodic expression of cln2. *PloS one*, 9(5):e96726, 2014.

[35] Guoxing Fu, Amit Sabnis, and Robert W Harrison. A deterministic-stochastic crossover algorithm for simulation of complex biochemical systems. In *Computational Advances in Bio and Medical Sciences (ICCABS), 2013 IEEE 3rd International Conference on*, pages 1–7. IEEE, 2013.

[36] Sten Rüdiger. Stochastic models of intracellular calcium signals. *Physics Reports*, 534(2):39–87, 2014.

[37] Johan Hattne, David Fange, and Johan Elf. Stochastic reaction-diffusion simulation with mesord. *Bioinformatics*, 21(12):2923–2924, 2005.

[38] Jeff Schulte, Rene Zeto, and David Roundy. MinD simulation github repository, 2015.

[39] Michael Kraus, Björn Wolf, and Bernhard Wolf. Crosstalk between cellular morphology and calcium oscillation patterns insights from a stochastic computer model. *Cell calcium*, 19(6):461–472, 1996.

[40] Daniel T Gillespie. Exact stochastic simulation of coupled chemical reactions. *The journal of physical chemistry*, 81(25):2340–2361, 1977.

[41] Bo Zhang, Josiane Zerubia, and Jean-Christophe Olivo-Marin. Gaussian approximations of fluorescence microscope point-spread function models. *Applied Optics*, 46(10):1819–1829, 2007.

[42] O Pierucci. Chromosome replication and cell division in escherichia coli at various temperatures of growth. *Journal of bacteriology*, 109(2):848–854, 1972.

[43] Jesse Stricker, Paul Maddox, ED Salmon, and Harold P Erickson. Rapid assembly dynamics of the escherichia coli ftsz-ring demonstrated by fluorescence recovery after photobleaching. *Proceedings of the National Academy of Sciences*, 99(5):3171–3175, 2002.

[44] N.D. Mermin. Thermal properties of the inhomogeneous electron gas. *Physical Review*, 137(5A):1441–1443, 1965.

[45] J.P. Hansen and I.R. McDonald. *Theory of Simple Liquids*. Elsevier Science, 2006.

[46] W.G. Chapman, K.E. Gubbins, G. Jackson, and M. Radosz. Saft: equation-of-state solution model for associating fluids. *Fluid Phase Equilibria*, 52:31–38, 1989.

[47] E. A. Müller and K. E. Gubbins. Molecular-based equations of state for associating fluids: A review of saft and related approaches. *Industrial & engineering chemistry research*, 40(10):2193–2211, 2001.

[48] Sugata P Tan, Hertanto Adidharma, and Maciej Radosz. Recent advances and applications of statistical associating fluid theory. *Industrial & Engineering Chemistry Research*, 47(21):8063–8082, 2008.

[49] Norman F Carnahan and Kenneth E Starling. Equation of state for nonattracting rigid spheres. *The Journal of Chemical Physics*, 51(2):635–636, 1969.

[50] GA Mansoori, NF Carnahan, KE Starling, and TW Leland Jr. Equilibrium thermodynamic properties of the mixture of hard spheres. *The Journal of Chemical Physics*, 54(4):1523–1525, 1971.

[51] WA Curtin and NW Ashcroft. Weighted-density-functional theory of inhomogeneous liquids and the freezing transition. *Physical review A*, 32(5):2909, 1985.

[52] Yaakov Rosenfeld. Free-energy model for the inhomogeneous hard-sphere fluid mixture and density-functional theory of freezing. *Physical review letters*, 63(9):980, 1989.

[53] Yaakov Rosenfeld, Dominique Levesque, and Jean-Jacques Weis. Free-energy model for the inhomogeneous hard-sphere fluid mixture: Triplet and higher-order direct correlation functions in dense fluids. *The Journal of Chemical Physics*, 92(11):6818–6832, 1990.

[54] P. Tarazona and Y. Rosenfeld. From zero-dimension cavities to free-energy functionals for hard disks and hard spheres. *Phys. Rev. E*, 55(5):R4873–R4876, May 1997.

[55] P Tarazona and Y Rosenfeld. Free energy density functional from 0d cavities. In *New Approaches to Problems in Liquid State Theory*, pages 293–302. Springer, 1999.

[56] P. Tarazona. Density functional for hard sphere crystals: A fundamental measure approach. *Phys. Rev. Lett.*, 84(4):694–697, Jan 2000.

[57] Pedro Tarazona. Fundamental measure theory and dimensional interpolation for the hard spheres fluid. *Physica A: Statistical Mechanics and its Applications*, 306:243–250, 2002.

[58] Y Rosenfeld, M Schmidt, H Löwen, and P Tarazona. Fundamental-measure free-energy density functional for hard spheres: dimensional crossover and freezing. *Physical Review E*, 55(4):4245, 1997.

[59] R. Roth, R. Evans, A. Lang, and G. Kahl. Fundamental measure theory for hard-sphere mixtures revisited: the White Bear version. *Journal of Physics: Condensed Matter*, 14:12063, 2002.

[60] H. Hansen-Goos and R. Roth. Density functional theory for hard-sphere mixtures: the white bear version mark ii. *Journal of Physics: Condensed Matter*, 18:8413, 2006.

[61] D. Fu and J. Wu. Vapor- Liquid Equilibria and Interfacial Tensions of Associating Fluids within a Density Functional Theory. *Ind. Eng. Chem. Res*, 44(5):1120–1128, 2005.

[62] P. Bryk, S. Sokołowski, and O. Pizio. Density functional theory for inhomogeneous associating chain fluids. *The Journal of chemical physics*, 125:024909, 2006.

[63] Jessica Hughes, Eric J Krebs, David Roundy, et al. A classical density-functional theory for describing water interfaces. *The Journal of chemical physics*, 138(2):024509–024509, 2013.

[64] Guillaume Jeanmairet, Maximilien Levesque, Rodolphe Vuilleumier, and Daniel Borgis. Molecular density functional theory of water. *The Journal of Physical Chemistry Letters*, 4(4):619–624, 2013.

[65] Shuangliang Zhao, Rosa Ramirez, Rodolphe Vuilleumier, and Daniel Borgis. Molecular density functional theory of solvation: From polar solvents to water. *The Journal of chemical physics*, 134:194102, 2011.

[66] Shuangliang Zhao, Zhehui Jin, and Jianzhong Wu. New theoretical method for rapid prediction of solvation free energy in water. *The Journal of Physical Chemistry B*, 115(21):6971–6975, 2011.

[67] Rosa Ramirez, Michel Mareschal, and Daniel Borgis. Direct correlation functions and the density functional theory of polar solvents. *Chemical physics*, 319(1):261–272, 2005.

[68] Rosa Ramirez and Daniel Borgis. Density functional theory of solvation and its relation to implicit solvent models. *The Journal of Physical Chemistry B*, 109(14):6754–6763, 2005.

[69] Maximilien Levesque, Virginie Marry, Benjamin Rotenberg, Guillaume Jeanmairet, Rodolphe Vuilleumier, and Daniel Borgis. Solvation of complex surfaces via molecular density functional theory. *The Journal of chemical physics*, 137:224107, 2012.

[70] Maximilien Levesque, Rodolphe Vuilleumier, and Daniel Borgis. Scalar fundamental measure theory for hard spheres in three dimensions: Application to hydrophobic solvation. *The Journal of Chemical Physics*, 137:034115, 2012.

[71] J. Lischner and TA Arias. Classical density-functional theory of inhomogeneous water including explicit molecular structure and nonlinear dielectric response. *The Journal of Physical Chemistry B*, 114(5):1946–1953, 2010.

[72] G.N.I. Clark, A.J. Haslam, A. Galindo, and G. Jackson. Developing optimal Wertheim-like models of water for use in Statistical Associating Fluid Theory (SAFT) and related approaches. *Molecular physics*, 104(22):3561–3581, 2006.

[73] G.J. Gloor, F.J. Blas, E.M. del Rio, E. de Miguel, and G. Jackson. A saft-dft approach for the vapour-liquid interface of associating fluids. *Fluid phase equilibria*, 194:521–530, 2002.

[74] G.J. Gloor, G. Jackson, F.J. Blas, E.M. Del Río, and E. de Miguel. An accurate density functional theory for the vapor-liquid interface of associating chain molecules based on the statistical associating fluid theory for potentials of variable range. *The Journal of chemical physics*, 121:12740, 2004.

[75] G.J. Gloor, G. Jackson, FJ Blas, E.M. del Río, and E. de Miguel. Prediction of the vapor-liquid interfacial tension of nonassociating and associating fluids with the saft-vr density functional theory. *The Journal of Physical Chemistry C*, 111(43):15513–15522, 2007.

[76] Khuloud Jaqaman, Kagan Tuncay, and Peter J. Ortoleva. Classical density functional theory of orientational order at interfaces: Application to water. *J. Chem. Phys.*, 120(2):926–938, 2004.

[77] G. N. Chuev and V. F. Sokolov. Hydration of hydrophobic solutes treated by the fundamental measure approach. *Journal of Physical Chemistry B*, 110(37):18496–18503, 2006.

[78] SB Kiselev and JF Ely. A new analytical formulation for the generalized corresponding states model for thermodynamic and surface properties in pure fluids. *Chemical Engineering Science*, 61(15):5107–5113, 2006.

[79] F.J. Blas, E.M. Del Río, E. De Miguel, and G. Jackson. An examination of the vapour-liquid interface of associating fluids using a saft-dft approach. *Molecular Physics*, 99(22):1851–1865, 2001.

[80] R. Sundararaman, K. Letchworth-Weaver, and T. A. Arias. A computationally efficacious free-energy functional for studies of inhomogeneous liquid water. *The Journal of chemical physics*, 137(4):044107–1–044107–6, 2012.

[81] M. S. Wertheim. Fluids with highly directional attractive forces. i. statistical thermodynamics. *Journal of statistical physics*, 35(1):19–34, 1984.

[82] M. S. Wertheim. Fluids with highly directional attractive forces. ii. thermodynamic perturbation theory and integral equations. *Journal of statistical physics*, 35(1):35–47, 1984.

[83] M. S. Wertheim. Fluids with highly directional attractive forces. iii. multiple attraction sites. *Journal of statistical physics*, 42(3):459–476, 1986.

[84] M. S. Wertheim. Fluids with highly directional attractive forces. iv. equilibrium polymerization. *Journal of statistical physics*, 42(3):477–492, 1986.

[85] Jeff B Schulte, Patrick A Kreitzberg, Chris V Haglund, and David Roundy. Using fundamental measure theory to treat the correlation function of the inhomogeneous hard-sphere fluid. *Physical Review E*, 86(6):061201, 2012.

[86] A. Gil-Villegas, A. Galindo, P.J. Whitehead, S.J. Mills, G. Jackson, and A.N. Burgess. Statistical associating fluid theory for chain molecules with attractive potentials of variable range. *The Journal of Chemical Physics*, 106:4168, 1997.

[87] J.A. Barker and D. Henderson. What is a "liquid"? understanding the states of matter. *Reviews of Modern Physics*, 48(4):587, 1976.

[88] David Chandler. Interfaces and the driving force of hydrophobic assembly. *Nature*, 437:640–647, 2005.

[89] Dietmar Paschek. Temperature dependence of the hydrophobic hydration and interaction of simple solutes: An examination of five popular water models. *The Journal of chemical physics*, 120:6674, 2004.

[90] Shekhar Jain, Aleksandra Dominik, and Walter G Chapman. Modified interfacial statistical associating fluid theory: A perturbation density functional theory for inhomogeneous complex fluids. *The Journal of chemical physics*, 127:244904, 2007.

[91] M. Plischke and D. Henderson. Pair correlation function in a fluid with density inhomogeneities: results of the percus-yevick and hypernetted chain approximations for hard spheres near a hard wall. *Proceedings of the Royal Society of London. A. Mathematical and Physical Sciences*, 404(1827):323–337, 1986.

[92] F. Lado. An efficient procedure for the study of inhomogeneous liquids. *Molecular Physics*, 107(4-6):301–308, 2009.

[93] A. González, FL Román, and JA White. A test-particle method for the calculation of the three-particle distribution function of the hard-sphere fluid: density functional theory and simulation. *Journal of Physics: Condensed Matter*, 11(19):3789, 1999.

[94] B Götzelmann, A Haase, and S Dietrich. Structure factor of hard spheres near a wall. *Physical Review E*, 53(4):3456, 1996.

[95] R Paul and S. J. Paddison. Variational methods for the solution of the ornstein-zernicke equation in inhomogeneous systems. *Physical Review E*, 67(1):016108, 2003.

[96] Søren Toxvaerd. Statistical mechanical and quasithermodynamic calculations of surface densities and surface tension. *Molecular Physics*, 26(1):91–99, 1973.

[97] Jeff Pressing and Joseph E Mayer. Surface tension and interfacial density profile of fluids near the critical point. *The Journal of Chemical Physics*, 59(5):2711–2722, 2003.

[98] SJ Salter and HT Davis. Statistical mechanical calculations of the surface tension of fluids. *The Journal of Chemical Physics*, 63(8):3295–3301, 2008.

[99] Vito Bongiorno and H Ted Davis. Modified van der waals theory of fluid interfaces. *Physical Review A*, 12:2213–2224, 1975.

[100] Søren Toxvaerd. Hydrostatic equilibrium in fluid interfaces. *Journal of Chemical Physics*, 64:2863–2867, 1976.

[101] MH Kalos, JK Percus, and M Rao. Structure of a liquid-vapor interface. *Journal of Statistical Physics*, 17(3):111–136, 1977.

[102] BS Carey, LE Scriven, and HT Davis. On gradient theories of fluid interfacial stress and structure. *The Journal of Chemical Physics*, 69(11):5040–5049, 2008.

[103] Thomas R Osborn and Clive A Croxton. Monotonic and oscillatory density profiles at the free liquid surface for simple atomic fluids. *Molecular Physics*, 40(6):1489–1502, 1980.

[104] BF McCoy, LE Scriven, and HT Davis. Comparison of molecular models of the liquid–vapor interface. *The Journal of Chemical Physics*, 75(9):4719–4726, 1981.

[105] Jonathan C Barrett. Some estimates of the surface tension of curved surfaces using density functional theory. *The journal of chemical physics*, 124(14):144705, 2006.

[106] Jonathan Harris and Stuart A Rice. Comment on the pair correlation function in an inhomogeneous liquid: A test of the fischer approximation. *The Journal of chemical physics*, 86(10):5731–5733, 1987.

[107] Zixiang Tang, LE Scriven, and HT Davis. Density-functional perturbation theory of inhomogeneous simple fluids. *The Journal of chemical physics*, 95(4):2659–2668, 1991.

[108] P Tarazona. Free-energy density functional for hard spheres. *Physical Review A*, 31(4):2672, 1985.

[109] T Wadewitz and J Winkelmann. Application of density functional perturbation theory to pure fluid liquid–vapor interfaces. *The Journal of Chemical Physics*, 113(6):2447–2455, 2000.

[110] J Winkelmann. The liquid-vapour interface of pure fluids and mixtures: application of computer simulation and density functional theory. *Journal of Physics: Condensed Matter*, 13(21):4739, 2001.

APPENDIX

A Evaluation of the functional derivatives in $g_\sigma^A(\mathbf{r})$

The expression for the asymmetric correlation function $g_\sigma^A(\mathbf{r})$ (Equation 4.19) involves the functional derivative $\frac{\delta A_{HS}}{\delta \sigma(\mathbf{r})}$. In this appendix we will explain how this derivative is evaluated. We begin by applying the chain rule in the following way:

$$\frac{\delta A_{HS}}{\delta \sigma(\mathbf{r})} = \int \left(\sum_\alpha \frac{\delta A_{HS}}{\delta n_\alpha(\mathbf{r}')} \frac{\delta n_\alpha(\mathbf{r}')}{\delta \sigma(\mathbf{r})} \right) d\mathbf{r}' \tag{A.1}$$

This expression requires us to evaluate $\frac{\delta A_{HS}}{\delta n_\alpha(\mathbf{r}')}$ and $\frac{\delta n_\alpha(\mathbf{r}')}{\delta \sigma(\mathbf{r})}$. The former is straightforward, given Equations 3.39-3.41, and we will write no more about it. The functional derivatives of the fundamental measures, however, require a bit more subtlety, and we will address them here.

We begin with the derivative of n_3, the filling fraction, which we will discuss in somewhat more detail than the remainder, which are similar in nature. Because the diameter $\sigma(\mathbf{r})$ is the diameter of a sphere *at position* $\boldsymbol{r}$, we write the fundamental measure $n_3(\mathbf{r}')$ as

$$n_3(\mathbf{r}') = \int n(\mathbf{r}'')\Theta\left(\frac{\sigma(\mathbf{r}'')}{2} - |\mathbf{r}' - \mathbf{r}''|\right) d\mathbf{r}'' \tag{A.2}$$

where we note that $\sigma(\mathbf{r}'')$ and $n(\mathbf{r}'')$ are the diameter and density, respectively, of spheres centered at position $\mathbf{r}''$. Thus the derivative with respect to the diameter of spheres at position $\mathbf{r}$ is

$$\frac{\delta n_3(\mathbf{r}')}{\delta\sigma(\mathbf{r})} = \frac{1}{2}\int n(\mathbf{r}'')\delta\left(\frac{\sigma(\mathbf{r}'')}{2} - |\mathbf{r}' - \mathbf{r}''|\right)\delta(\mathbf{r} - \mathbf{r}'')d\mathbf{r}'' \tag{A.3}$$

$$= n(\mathbf{r})\delta(\sigma(\mathbf{r})/2 - |\mathbf{r}' - \mathbf{r}|) \tag{A.4}$$

This pattern will hold for each fundamental measure: because we are seeking the change in free energy when spheres at point $\mathbf{r}$ are expanded, the integral over density is eliminated. To compute the correlation funtion g_σ^A, we convolve this delta function with the product of the density and a local derivative of $\Phi(\mathbf{r})$:

$$\frac{\delta A_{HS}}{\delta\sigma(\mathbf{r})} = \int \frac{\partial\Phi(\mathbf{r}')}{\partial n_3(\mathbf{r}')} n(\mathbf{r}')\delta(\sigma/2 - |\mathbf{r}' - \mathbf{r}|)d\mathbf{r}' + \cdots \tag{A.5}$$

As we shall see, there are only four convolution kernels, leading to four additional convolutions beyond those required for FMT.

The functional derivative of n_2 introduces our second convolution kernel, which is a derivative of the delta function.

$$\frac{\delta n_2(\mathbf{r}')}{\delta\sigma(\mathbf{r})} = \frac{1}{2}n(\mathbf{r})\delta'(\sigma(\mathbf{r})/2 - |\mathbf{r}' - \mathbf{r}|) \tag{A.6}$$

The derivatives of the remaining scalar densities n_1 and n_0 reduce to sums of the terms above:

$$\frac{\delta n_1(\mathbf{r}')}{\delta\sigma(\mathbf{r})} = \frac{n(\mathbf{r})}{4\pi\sigma(\mathbf{r})}\delta'(\sigma(\mathbf{r})/2 - |\mathbf{r}' - \mathbf{r}|) - \frac{n(\mathbf{r})}{2\pi\sigma(\mathbf{r})^2}\delta(\sigma(\mathbf{r})/2 - |\mathbf{r}' - \mathbf{r}|) \tag{A.7}$$

and

$$\frac{\delta n_0(\mathbf{r}')}{\delta\sigma(\mathbf{r})} = \frac{n(\mathbf{r})}{2\pi\sigma(\mathbf{r})^2}\delta'(\sigma(\mathbf{r})/2 - |\mathbf{r}' - \mathbf{r}|) - 2\frac{n(\mathbf{r})}{\pi\sigma(\mathbf{r})^3}\delta(\sigma(\mathbf{r})/2 - |\mathbf{r}' - \mathbf{r}|) \tag{A.8}$$

The vector-weighted densities $\mathbf{n}_{V1}$ and $\mathbf{n}_{V2}$ give terms analogous to those of n_1 and n_2:

$$\frac{\delta \mathbf{n}_{V2}(\mathbf{r}')}{\delta\sigma(\mathbf{r})} = -\frac{1}{2}n(\mathbf{r})\delta'(\sigma(\mathbf{r})/2 - |\mathbf{r}' - \mathbf{r}|)\frac{\mathbf{r} - \mathbf{r}'}{|\mathbf{r} - \mathbf{r}'|} \tag{A.9}$$

$$\begin{aligned}\frac{\delta \mathbf{n}_{V1}(\mathbf{r}')}{\delta\sigma(\mathbf{r})} = &-\frac{n(\mathbf{r})}{4\pi\sigma(\mathbf{r})}\delta'(\sigma(\mathbf{r})/2 - |\mathbf{r}' - \mathbf{r}|)\frac{\mathbf{r} - \mathbf{r}'}{|\mathbf{r} - \mathbf{r}'|} \\ &+ \frac{n(\mathbf{r})}{2\pi\sigma(\mathbf{r})^2}\delta(\sigma(\mathbf{r})/2 - |\mathbf{r}' - \mathbf{r}|)\frac{\mathbf{r} - \mathbf{r}'}{|\mathbf{r} - \mathbf{r}'|}\end{aligned} \tag{A.10}$$

Thus there are four convolution kernels used in computing g_σ^A: one scalar and one vector delta function, and one scalar and one vector derivative of the delta function.